INTERNATIONAL JOURNAL OF
NUMERICAL ANALYSIS AND MODELING
Volume 9, Number 3, Pages 745–776

DERIVATION OF VERTICAL EQUILIBRIUM MODELS FOR CO_2 MIGRATION FROM PORE SCALE EQUATIONS

WILLIAM G. GRAY, PAULO A. HERRERA, SARAH E. GASDA, AND HELGE K. DAHLE

This paper is dedicated to Magne Espedal.

Abstract. Equations describing flow in porous media averaged to allow for lateral spatial variability but integrated over the vertical dimension are derived from pore scale equations. Under conditions of vertical equilibrium, the equations are simplified and employed to describe migration of CO_2 injected into an aquifer of variable thickness. The numerical model based on the vertical equilibrium equations is shown to agree well with a fully three-dimensional model. Trapping of CO_2 in undulations at the top of the aquifer is shown to retard CO_2 migration.

Key words. vertical equilibrium, carbon sequestration, multiphase flow, porous media, numerical simulation, ECLIPSE

1. Introduction

Storage of carbon dioxide (CO_2) in saline aquifers has been proposed as an alternative to reduce greenhouse gas emissions [5, 45]. It is expected that injection rates of several million tons per year will be required to capture the emissions from one or several industrial point sources [1]. Detailed modeling and numerical simulations will be required to evaluate the storage capacity of potential sequestration sites, to assess the feasibility of injecting such high volume rates and to predict the long-term fate of the injected CO_2 [6]. In particular, quantitative predictions of migration distances and estimates of time scales associated with different trapping mechanisms will be essential in assessing possible risks associated with CO_2 storage [45].

Supercritical CO_2 injection and subsequent storage in saline aquifers involves physical and chemical trapping mechanisms that occur over several length and time scales. During the injection period, CO_2 quickly rises due to its lower density with respect to the resident brine. Once it reaches an impermeable sealing layer at the top of the aquifer it accumulates beneath it [4, 29]. This structural entrapment of CO_2 is the primary trapping mechanism during the injection time frame. Once injection ceases and the driving pressure dissipates, CO_2 will migrate due to buoyancy forces alone, following the upslope dip of the caprock [4, 31, 48]. During this period, CO_2 will become gradually immobilized due to irregularities in the caprock surface and other primary trapping processes such as residual and solubility trapping [38, 45]. Mineralization occurs on much longer time scales than the primary mechanisms [35, 45], and thus is a secondary process not considered further here. Characterization of the primary post-injection trapping processes is essential for

Received by the editors June 9, 2011 and, in revised form, August 16, 2011.

This work was supported by National Science Foundation grant ATM-0941235 and Department of Energy grant DE-SC0002163. Support of the U. S. Fulbright Foundation and the Center for Integrated Petroleum Research at the University of Bergen for WGG is gratefully acknowledged. The contribution of PAH and HKD was supported by the Norwegian Research Council, Statoil AS and Norske Shell as part of the Geological Storage of CO_2: Mathematical Modelling and Risk Analysis (MatMoRA) project (project no. 178013). SEG is supported by a King Abdullah University of Science and Technology Research Fellowship.

understanding the long-term fate of CO_2 in the subsurface over the thousand years time scale. However, because of the large spatial and temporal scales that must be considered, traditional numerical approaches to this problem are impractical in terms of computational requirements. Therefore, efficient mathematical modeling approaches are needed to speed up simulations [6].

With the objective of developing effective models, certain physical characteristics of the CO_2-brine system can be exploited to simplify the governing system of equations. For example, given the strong buoyancy forces, it is reasonable to assume that complete gravity segregation occurs quickly during and after the injection period. In addition, the large horizontal and thin vertical scales result in negligible vertical movement of the fluids. These characteristics lead to implementation of what is known as the vertical equilibrium (VE) assumption. This assumption facilitates vertical integration of the three-dimensional governing flow equations to obtain a set of two-dimensional equations [39, 49, 56]. So called vertically-integrated or VE models have been used extensively in the past to simulate the behavior of petroleum reservoirs where strong vertical fluid segregation occurs [9, 10, 13, 19, 39, 44, 55], or groundwater aquifers with large aspect ratios [2, 20]. VE models have received renewed attention in recent years to model CO_2 injection and migration in saline aquifers [12, 22, 31, 36, 43, 47, 49, 51]. Despite the model simplifications, analytical and numerical solutions to VE models have compared well with solutions using standard simulation tools [12, 49, 51], most notably in two recent benchmark studies [8, 50]. Recently, Nilsen et al. [48] simulated the long-term migration of CO_2 injected at the Utsira formation in the North Sea [7]. Furthermore, because of their infinite vertical resolution, VE models have proven to be particularly advantageous for modeling the long-term movement of thin CO_2 plumes underneath the aquifer caprock [31, 32, 48].

As with any simplified model, the VE model is not appropriate for all systems. The limitations become important when considering small-scale (in the tens of meters) or short-term ($<$10 yrs) processes, particularly when anisotropy and intermediate shale layers retard the vertical migration of the CO_2 plume. For example, it has been shown that the VE model leads to inaccurate results when examining near wellbore flow effects of CO_2 injection [42]. Therefore, we focus on the longer term effects of CO_2 migration over tens of kilometers after injection has ceased, an application for which the VE model is appropriate.

Previous mathematical models based on the VE assumption have been developed from the standard Darcy theory of two-phase flow, e.g.[31, 39]. By this process Darcy scale, or macroscale equations, are integrated over the thickness of the flow domain. The macroscale equations are employed as a starting point for a change in scale to the megascale, the fully integrated scale. Here, we begin with the microscale equations. These equations can be integrated to the macroscale to obtain multiphase flow equations in term of variables that are well-defined functions of their microscale precursors for multiphase flow. This procedure is best carried out when the conservation equations of mass, momentum, and energy, along with the fundamental thermodynamic postulates, are integrated to the macroscale [34]. These constructed equations and closure conditions would then have to be integrated over the vertical to obtain a VE set. An alternative approach to obtaining the VE equation is to start with the microscale equations and, in one step, integrate the conservation and thermodynamic relations to a form that is macroscopic in the lateral direction and megascale in the vertical direction. This is accomplished by using the theorems for mixed megascale/macroscale averaging [25]. We note that the

use of available theorems to obtain a set of equations that is completely megascopic has been advanced recently [26]. The present development seems to be the first for obtaining mixed macroscale/megascale equations. The advantage of this approach is that the need to develop approximate closure relations at the macroscale is bypassed. Rather, all closure relations and parameters are defined directly at the scales of the problem of interest. For the present study, we reduce the equations to forms previously employed for VE models (e.g., [22, 31, 36, 39]), but we are also explicitly aware of all assumptions that have gone into the equations, definition of variables, and assumptions in the closure relations.

An important aspect of confirming the effectiveness of the VE equations for modeling is verification against standard simulation tools that solve the fully three-dimensional macroscale equations in realistic geologic systems. In previous studies, these types of systems have been the subject of a benchmark comparison [8] and a recent study of the Utsira formation [48]. In the former study, several institutional and commercial codes, including a VE model [22], were applied to a hypothetical injection/post-injection scenario in the Johansen formation, a heterogeneous formation that is structurally characterized by a dipping, non-flat top surface. Although a strict comparison was not performed in this case, the VE model produced qualitatively similar results to the three-dimensional simulators. In the latter study, the Sleipner injection site [7] was modeled using a VE model and then compared with ECLIPSE 3D simulations [48]. The VE simulations were shown to compare favorably to full three-dimensional simulations of CO_2 migration in real aquifers. However, the primary goal was to validate the VE and 3D models against observed data. The results of this work identified caprock topography as a feature that greatly impacted the validation. In addition, the VE model was able to match the observed data better than the ECLIPSE 3D simulations, which was attributed to difficulty in obtaining sufficient vertical resolution with the ECLIPSE 3D simulator.

Much of the recent research on the long-term fate of CO_2 in saline aquifers has focused on solubility and residual trapping mechanisms. For example, recent publications emphasized the role of the aquifer slope, regional background flow and residual trapping on the migration distance and plume speed [31, 33, 36, 37]. Other studies have investigated the role of the capillary fringe and show that it may reduce the tip speed of the CO_2 plume significantly for systems with strong capillary effects [24, 33, 50]. And finally, recent studies have examined the process of convection-driven CO_2 dissolution into brine using high-resolution numerics and/or analytical methods [18, 28, 41, 46, 52, 53]. This enhanced dissolution phenomenon has recently been incorporated into the vertically-integrated framework and used to simulate its impact on large scale CO_2 storage systems [23]. On the other hand, with the exception of brief discussions in few studies (e.g. [40]), structural trapping has received much less attention even though experience gained in hydrocarbon exploration [11], would indicate that it may represent the largest potential trapping volume in the reservoir. Moreover, structural trapping takes place at much shorter time scales than the other three mechanisms so that it controls the plume evolution during the first several hundred years. For example, Nilsen et al. [48] demonstrated the importance of correctly modeling the caprock topography for understanding the observed plume spreading at the Utsira Sand aquifer. Despite the potentially significant impact of irregular caprocks, no other study has addressed the effect on structural trapping and long-term CO_2 migration. The present study is motivated by the desire to examine VE models in simulating CO_2 migration in synthetic aquifers with irregular caprock topography. We compare results of VE models

with full 3D simulations to demonstrate the applicability of VE models to simulate irregular caprock scenarios. In addition, we analyze the simulation results to shed light on the influence of caprock geometry on plume migration distance and speed. In a subsequent manuscript, we will use those results as the main motivation to develop effective equations that account for sub-scale heterogeneity in the caprock topography.

This manuscript has three main objectives: i) to present a rigorous derivation of the VE equations for modeling CO_2 migration in saline aquifers; ii) to verify the suitability of VE formulations to simulate CO_2 migration in aquifers with irregular caprock; and iii) to study the effect of caprock topography on the intermediate to long term CO_2 movement.

2. Averaged Porous Media Equations

In this section, we will develop averaged porous media equations that can be used to model two-dimensional lateral migration of a non-wetting CO_2 phase, designated as the n phase, into a brine-saturated w phase. The model formulation will be presented starting with the three-dimensional microscale equations for mass and momentum conservation. These equations will be integrated over a spatial region, Ω, that is a cylinder whose height is denoted as b such that the size of the averaging volume is $b\pi(\Delta r)^2$ where Δr is the macroscale lateral averaging length scale and $A = \pi(\Delta r)^2$ is the cross-sectional area of the cylinder. Here, the microscale is defined to be at the scale of individual pores, the macroscale is the averaging scale in the lateral direction of order Δr, while the megascale is the scale of the aquifer height. Thus the resultant spatially integrated equations are macroscopic in the lateral directions but megascopic in the vertical direction. Because the equations have both macroscale and megascale elements, they will be referred to, for convenience, as being at the averaged scale. The averaging theorems required to perform the integration to obtain the appropriate conservation equations with these scale characteristics are from the $[3, (2, 0), 1]$ family [25], which are described in more detail in Appendix A.

To begin, we will summarize the derivation framework as well as identify and describe the assumptions employed in the model development at both at the microscale and averaged scale. These assumptions are not necessary for transformation of the three-dimensional microscale equations to the larger scales and may be relaxed depending on the system of interest.

2.1. Microscale System and Assumptions. We begin with a microscale system of mass and momentum conservation equations for both the n and w phases. At the microscale, certain simplifying assumptions are invoked to facilitate the model derivation. First, we will assume that mass transfer between phases is negligible and that no mass accumulates at the interfaces between phases. Thus, the mass density of the interfaces, mass per unit area, is zero; and no mass conservation equation for the interface need be developed. In addition, we consider the solid grains to be fixed with zero velocity. And finally, we consider each fluid to be Newtonian with relatively slow velocities and negligible intra-fluid viscous effects.

Each of these assumptions will be applied throughout the derivation with a discussion of their effect on the equation development. We emphasize that these assumptions are not necessary to perform the derivation, and may not be valid for all systems. For instance, we have only considered an isothermal system and have not written an energy conservation equation for this system. In some cases, it

will be necessary to integrate energy along with mass and momentum conservation equations, but that is beyond the scope of this current work.

2.2. Averaged Scale System and Assumptions. The objective of the derivation is to arrive at an averaged scale system of mass and momentum conservation equations for a post-injection segregated CO_2-brine system, such as depicted in Fig 1. In this figure, three regions are depicted in order from bottom to top: 1) the brine region, 2) the brine region with residual CO_2; and 3) the CO_2 region with residual brine. The flow domain is confined on top and bottom by an impermeable boundary. Assuming that the vertical direction z is positive upwards in a direction orthogonal to the bottom of the flow domain, and there exists a constant datum $z = 0$, we observe that the vertical organization of fluids can be described by the vertical coordinates of three interfaces by noting that

$$H \geq h \geq h_i \geq 0. \tag{1}$$

In eqn (1), $H(x, y)$ is the upper boundary of the flow domain, or the aquifer height, $h(x, y, t)$ is the location of the interface between saturated CO_2 and brine (with or without residual CO_2), and $h_i(x, y, t)$ is the location of the interface between brine with residual CO_2 and saturated brine.

In the region 1, only brine exists at a saturation of $s^w = 1$. Because there is no CO_2 in this region, the mobility of brine will be higher in this region than in the other two regions. In region 2, there is a history of complete drainage and imbibition of brine to a residual CO_2 saturation, s^n_{res}. The residual CO_2 is no longer mobile, and the mobility of the brine phase will be that obtained at the saturation $s_w = 1 - s^n_{\text{res}}$. Finally, the brine that originally saturated region 3 has been partially displaced by CO_2 to residual brine saturation, s^w_{res}. Only CO_2 is mobile in this region and is present at a saturation $s^n = 1 - s^w_{\text{res}}$. These properties of each of the three regions are summarized in Table 1. Implied in Fig 1 and Table 1 is the assumption that the saturations obtained from averaging, that will be functions of lateral coordinates and time, will be constant within each region.

A key feature of the averaged system we wish to describe is the assumption of complete gravity segregation due to buoyancy. This assumption implies that vertical buoyancy forces are dominant and the timescale to gravity segregation is fast relative to lateral flow velocities [56]. For many CO_2-brine systems, density differences are significant, and thus this assumption is typically valid. In addition, the timescale of lateral flow is quite large during the post-injection period, with only a few meters per year of migration expected for many systems.

One of the main objectives of this derivation is to develop a set of averaged equations from first principles that are megascale in the vertical direction and macroscale in the lateral directions. Certain assumptions appropriate for the system under consideration will be made to ease the derivation, and eliminate terms in some cases, but these assumptions are not, in general, necessary. One advantage of the rigorous process employed is that we obtain the particular set of conditions for which certain assumptions are valid. For instance, it is common to invoke the assumption that the fluids depicted in Fig 1 are in vertical equilibrium (VE), which means that flow is predominantly horizontal and vertical flow is negligible and may be ignored. We will derive the averaged equations without assuming VE, thus obtaining all three vector components of the vertically-megascopic momentum equation From this point, we can extract the vertical momentum component and obtain the criteria under which the VE assumption may be justified.

The concept of vertical equilibrium is commonly applied in groundwater and other subsurface applications, wherever the lateral length scale is much larger than the vertical scale of the system [39, 56]. Thus, VE may be considered an appropriate assumption for most CO_2 injection scenarios into long, thin aquifers [22, 49]. The simplification to the system facilitated when the VE assumption applies is that the pressure distribution is vertically static. For instance, for the case of a single-phase groundwater system, the VE condition is known as the Dupuit assumption and the vertical pressure distribution is simply defined as hydrostatic. The VE assumption is also an important element of the classic Ghyben-Herzberg relation that approximates a fresh water lens overlying sea water as a two phase system [15, 16, 30]. For a two-phase system, the location of the phases must be known to define the vertical distribution of pressure. Because we have assumed gravity segregation, the vertical pressure is tied to the density of the n phase in region 1 and the density of the w phase in regions 2 and 3. As such, gravity segregation is closely tied to the concept of vertical equilibrium [56]. Related to gravity segregation and vertical equilibrium is the assumption of a sharp interface between the two fluid phases [49]. In Fig 1, the curve indicating the lower boundary of region 3 is the location at which a jump change in CO_2 saturation occurs from $s^n = 1 - s^w_{\text{res}}$ in region 3 to s^n_{res} in region 2 or $s^n = 0$ in region 1. In real systems, we expect that capillary forces will act locally at this interface, dispersing the fluids and creating a transition zone in saturation, known as a capillary fringe, where both phases exist and are mobile. The sharp interface assumption considers the transition zone to be negligibly small relative to the height of the aquifer. It should be noted that a sharp interface is not a requirement in order to perform the vertical integration. In the case of a large transition zone, we may assume that vertical equilibrium still exists if the timescale to equilibrium between capillary and buoyancy forces is short relative to that for horizontal flow [24]. Once the integration is performed, the vertical distribution in saturation can be recovered since it is well defined by the local capillary pressure function at equilibrium. This case has been studied more extensively by [50] and applied by [23], and will not be discussed further here.

As mentioned, the vertical direction for megascale averaging, which is denoted in Fig 1 by the unit vector $\mathbf{\Lambda}$, is normal to the bottom boundary. For many natural sedimentary systems, the large-scale topography of the aquifer top and bottom boundaries is not uniformly flat or horizontal in space (i.e. [7, 17]). There is variation at all spatial scales. Here, we are concerned with two scales. First, there is the basin-scale topography that can be characterized over hundreds of kilometers by a formation dip angle θ, that is usually on the order of 1° [1, 21, 31]. In this case, $\mathbf{\Lambda}$ can be defined as a unit vector orthogonal to the large-scale dip of the formation, which is the definition adopted in this formulation. This angle may change slowly over the lateral extent of the aquifer, in which case the corresponding spatial variation in $\mathbf{\Lambda}$ can be considered. On the other hand, there is often significant variation in topography at the scale of tens or hundreds of meters. At such a scale, called the regional scale, the boundary between the formation and the overlying caprock may be characterized by dome structures, traps and other local fluctuations from the basin-scale dip angle of the aquifer. This local change in topography may be accounted for through gradients in the top surface of the aquifer, although the direction of $\mathbf{\Lambda}$ in deriving the equations will not change.

2.3. Mathematical Derivation. The porous medium is composed of phases and interfaces between phases, as well as common curves where three phases meet. We will refer to all of these as entities. We will be concerned with averaging of phase

properties. For convenience, a subscript will be used to indicate a microscale property while a superscript will denote a property averaged to the macroscale. Further description of averaging theorems is provided in Appendix A and a summary of the notation is included in Appendix B. These theorems are applied to the equations of mass and momentum conservation for the fluid phases.

2.4. Mass Conservation Equation. The microscale equation of mass conservation of the brine or CO_2 phase is

$$\frac{\partial \rho_\alpha}{\partial t} + \nabla \cdot (\rho_\alpha \mathbf{v}_\alpha) = 0 \qquad \alpha = \{w, n\}. \tag{2}$$

Integration of this equation over the α phase then yields

$$\left\langle \frac{\partial \rho_\alpha}{\partial t} \right\rangle_{\Omega_\alpha,\Omega} + \langle \nabla \cdot (\rho_\alpha \mathbf{v}_\alpha) \rangle_{\Omega_\alpha,\Omega} = 0 \qquad \alpha = \{w, n\}. \tag{3}$$

Multiplication by the height of the region being considered, b, and application of eqn (73) to the first term and eqn (74) to the second term yields the averaged mass conservation equation

$$\begin{aligned} &\frac{\partial'}{\partial t}\left(b\epsilon^\alpha \rho^\alpha\right) + \nabla' \cdot \left(b\epsilon^\alpha \rho^\alpha \mathbf{v}^{\overline{\alpha}\prime}\right) + \sum_{\kappa \in \mathcal{I}_{c\alpha}} b\langle \rho_\alpha \left(\mathbf{v}_\alpha - \mathbf{v}_\kappa\right) \cdot \mathbf{n}_\alpha \rangle_{\Omega_\kappa,\Omega} \\ &\qquad + \sum_{\text{ends}} b\langle \rho_\alpha \left(\mathbf{v}_\alpha - \mathbf{w}_{\text{end}}\right) \cdot \mathbf{n}_\alpha \rangle_{\Omega_{\alpha_{\text{end}}},\Omega} = 0, \end{aligned} \tag{4}$$

where ϵ^α is the volume fraction of the α phase. This equation is megascopic in the vertical direction and macroscopic in the lateral direction. The first summation in this expression accounts for interphase transfer and the second summation accounts for fluxes at the top and bottom of the averaging domain. Because there is assumed to be no phase change, the interface exchange terms may be deleted. Thus, eqn (4) becomes

$$\frac{\partial'}{\partial t}\left(b\epsilon^\alpha \rho^\alpha\right) + \nabla' \cdot \left(b\epsilon^\alpha \rho^\alpha \mathbf{v}^{\overline{\alpha}\prime}\right) + \sum_{\text{ends}} b\langle \rho_\alpha \left(\mathbf{v}_\alpha - \mathbf{w}_{\text{end}}\right) \cdot \mathbf{n}_\alpha \rangle_{\Omega_{\alpha_{\text{end}}},\Omega} = 0. \tag{5}$$

When the averaged density is constant, it may be removed from the derivatives in the first two terms. If, additionally, this constant value is equal to the microscale density at the top and bottom of the averaging domain, which would be the case if the microscale density is constant, this equation simplifies further by dividing by the density to obtain

$$\frac{\partial'}{\partial t}\left(b\epsilon^\alpha\right) + \nabla' \cdot \left(b\epsilon^\alpha \mathbf{v}^{\overline{\alpha}\prime}\right) + \sum_{\text{ends}} b\langle \left(\mathbf{v}_\alpha - \mathbf{w}_{\text{end}}\right) \cdot \mathbf{n}_\alpha \rangle_{\Omega_{\alpha_{\text{end}}},\Omega} = 0. \tag{6}$$

In this study, since the solid grains have been assumed to be immobile, the average Darcy velocity may be defined as

$$\mathbf{q}^{\overline{\overline{\alpha}\prime}} = \epsilon^\alpha \mathbf{v}^{\overline{\alpha}\prime}. \tag{7}$$

For the fluid phases we can make use of the saturation whereby

$$\epsilon s^\alpha = \epsilon^\alpha \qquad \alpha = \{w, n\}, \tag{8}$$

where ϵ is porosity. Thus it follows that

$$s^w + s^n = 1. \tag{9}$$

The mass conservation equation for a fluid in each vertically integrated region will then be

$$\frac{\partial'}{\partial t}\left(b\epsilon s^{\alpha}\right)+\nabla'\cdot\left(b\mathbf{q}^{\overline{\overline{\alpha}}\prime}\right)+\sum_{\text{ends}} b\langle\left(\mathbf{v}_{\alpha}-\mathbf{w}_{\text{end}}\right)\cdot\mathbf{n}_{\alpha}\rangle_{\Omega_{\alpha_{\text{end}}},\Omega}=0. \tag{10}$$

Note that in this equation, only the lateral components of the averaged Darcy velocity appear. No assumption is made about whether the vertical velocity is zero, only that the direction of the vertical is independent of space and time.

Eqn (10) can be applied directly as a vertically megascale and laterally macroscale mass conservation equation for the w and n fluids in regions 1, 2, or 3 defined previously. We will here add the equations appropriate for a phase at any location over the three regions. Note that the mass exchange terms at the tops and bottoms will cancel out at interfaces between regions and are specified to be zero at the top and bottom of the study domain. We will consider the porosity to be a constant so that for the w phase we obtain

$$\begin{aligned}&\frac{\partial'}{\partial t}\left\{\epsilon\left[h_i+\left(h-h_i\right)\left(1-s^{n}_{\text{res}}\right)+\left(H-h\right)s^{w}_{\text{res}}\right]\right\}\\&\qquad+\nabla'\cdot\left[h_i\mathbf{q}_1^{\overline{\overline{w}}\prime}+\left(h-h_i\right)\mathbf{q}_2^{\overline{\overline{w}}\prime}\right]=0,\end{aligned} \tag{11}$$

where we have made use of the fact that the w phase is immobile in region 3. For the n phase we have

$$\begin{aligned}&\frac{\partial'}{\partial t}\left\{\epsilon\left[\left(h-h_i\right)s^{n}_{\text{res}}+\left(H-h\right)\left(1-s^{w}_{\text{res}}\right)\right]\right\}\\&\qquad+\nabla'\cdot\left[\left(H-h\right)\mathbf{q}_3^{\overline{\overline{n}}\prime}\right]=0.\end{aligned} \tag{12}$$

In this equation, we have made use of the fact that there is no n phase in region 1 and that n phase mobility is zero in region 2.

The forms of eqns (11) and (12) suggest that we make the following definitions of vertically averaged saturations, S^{α}, and lateral velocities, $\mathbf{Q}^{\overline{\overline{\alpha}}\prime}$:

$$S^{\alpha}=\frac{h_i s_1^{\alpha}+\left(h-h_i\right)s_2^{\alpha}+\left(H-h\right)s_3^{\alpha}}{H}, \tag{13}$$

and

$$\mathbf{Q}^{\overline{\overline{\alpha}}\prime}=\frac{h_i\mathbf{q}_1^{\overline{\overline{\alpha}}\prime}+\left(h-h_i\right)\mathbf{q}_2^{\overline{\overline{\alpha}}\prime}+\left(H-h\right)\mathbf{q}_3^{\overline{\overline{\alpha}}\prime}}{H}. \tag{14}$$

From eqn (13), it follows that the vertically-averaged saturations must sum to unity, which is analogous to eqn (9),

$$S^{w}+S^{n}=1. \tag{15}$$

Thus mass conservation eqns (11) and (12) may be written

$$\frac{\partial'}{\partial t}\left(\epsilon H S^{\alpha}\right)+\nabla'\cdot\left(H\mathbf{Q}^{\overline{\overline{\alpha}}\prime}\right)=0 \qquad \alpha=\{w,n\}. \tag{16}$$

Since ϵ and H are independent of time, this equation may alternatively be written

$$\epsilon H\frac{\partial' S^{\alpha}}{\partial t}+\nabla'\cdot\left(H\mathbf{Q}^{\overline{\overline{\alpha}}\prime}\right)=0 \qquad \alpha=\{w,n\}. \tag{17}$$

From summation of this equation over the w and n phases in light of the condition given in eqn (15) we see that

$$\nabla'\cdot\left[H\left(\mathbf{Q}^{\overline{\overline{w}}\prime}+\mathbf{Q}^{\overline{\overline{n}}\prime}\right)\right]=0. \tag{18}$$

A hysteresis model is required to relate the quantities h and h_i that appear in eqns (13) and (14). Making use of the fact that $h \geq h_i$, the macroscale interface between region 1 and 2 can be modeled as

$$h_i = \min_t(h). \tag{19}$$

2.5. Momentum Conservation Equation. The microscale equation for conservation of momentum of the α phase is

$$\frac{\partial(\rho_\alpha \mathbf{v}_\alpha)}{\partial t} + \nabla\cdot(\rho_\alpha \mathbf{v}_\alpha \mathbf{v}_\alpha) - \nabla\cdot\mathbf{t}_\alpha - \rho_\alpha \mathbf{g} = 0. \tag{20}$$

Integration of this equation over the phase within an averaging region then yields

$$\left\langle \frac{\partial(\rho_\alpha \mathbf{v}_\alpha)}{\partial t} \right\rangle_{\Omega_\alpha,\Omega} + \langle \nabla\cdot(\rho_\alpha \mathbf{v}_\alpha \mathbf{v}_\alpha)\rangle_{\Omega_\alpha,\Omega} - \langle \nabla\cdot\mathbf{t}_\alpha\rangle_{\Omega_\alpha,\Omega} - \langle \rho_\alpha \mathbf{g}\rangle_{\Omega_\alpha,\Omega} = 0. \tag{21}$$

Multiplication by b and application of eqn (73) to the first term and eqn (74) to the second and third terms yields

$$\begin{aligned} &\frac{\partial'}{\partial t}\left(b\epsilon^\alpha \rho^\alpha \mathbf{v}^{\overline{\alpha}}\right) + \nabla'\cdot\left(b\epsilon^\alpha \rho^\alpha \mathbf{v}^{\overline{\alpha}}\mathbf{v}^{\overline{\alpha}}\right) - \nabla'\cdot\left(b\epsilon^\alpha \mathbf{t}^{\overline{\overline{\alpha}}\prime}\right) - b\epsilon^\alpha \rho^\alpha \mathbf{g} \\ &\qquad + \sum_{\kappa\in\mathcal{I}_{c\alpha}} b\langle[\rho_\alpha \mathbf{v}_\alpha(\mathbf{v}_\alpha - \mathbf{v}_\kappa) - \mathbf{t}_\alpha]\cdot\mathbf{n}_\alpha\rangle_{\Omega_\kappa,\Omega} \\ &\qquad + \sum_{\text{ends}} b\langle[\rho_\alpha \mathbf{v}_\alpha(\mathbf{v}_\alpha - \mathbf{w}_{\text{end}}) - \mathbf{t}_\alpha]\cdot\mathbf{n}_\alpha\rangle_{\Omega_{\alpha_{\text{end}}},\Omega} = 0, \end{aligned} \tag{22}$$

where

$$\epsilon^\alpha \mathbf{t}^{\overline{\overline{\alpha}}\prime} = (\mathbf{I} - \mathbf{\Lambda}\mathbf{\Lambda})\cdot\left\langle \mathbf{t}_\alpha - \rho_\alpha\left(\mathbf{v}_\alpha - \mathbf{v}^{\overline{\alpha}}\right)\left(\mathbf{v}_\alpha - \mathbf{v}^{\overline{\alpha}}\right)\right\rangle_{\Omega_\alpha,\Omega}. \tag{23}$$

When there is no interphase mass exchange, eqn (22) simplifies to

$$\begin{aligned} &\frac{\partial'}{\partial t}\left(b\epsilon^\alpha \rho^\alpha \mathbf{v}^{\overline{\alpha}}\right) + \nabla'\cdot\left(b\epsilon^\alpha \rho^\alpha \mathbf{v}^{\overline{\alpha}}\mathbf{v}^{\overline{\alpha}}\right) - \nabla'\cdot\left(b\epsilon^\alpha \mathbf{t}^{\overline{\overline{\alpha}}\prime}\right) - b\epsilon^\alpha \rho^\alpha \mathbf{g} \\ &\qquad - \sum_{\kappa\in\mathcal{I}_{c\alpha}} b\langle \mathbf{t}_\alpha\cdot\mathbf{n}_\alpha\rangle_{\Omega_\kappa,\Omega} + \sum_{\text{ends}} b\langle[\rho_\alpha \mathbf{v}_\alpha(\mathbf{v}_\alpha - \mathbf{w}_{\text{end}}) - \mathbf{t}_\alpha]\cdot\mathbf{n}_\alpha\rangle_{\Omega_{\alpha_{\text{end}}},\Omega} = 0. \end{aligned} \tag{24}$$

We can apply the product rule to the first two terms in eqn (24) and then substitute in mass conservation eqn (5) to simplify the momentum equation to

$$\begin{aligned} &b\epsilon^\alpha \rho^\alpha \frac{\partial' \mathbf{v}^{\overline{\alpha}}}{\partial t} + b\epsilon^\alpha \rho^\alpha \mathbf{v}^{\overline{\alpha}}\cdot\nabla'\mathbf{v}^{\overline{\alpha}} - \nabla'\cdot\left(b\epsilon^\alpha \mathbf{t}^{\overline{\overline{\alpha}}\prime}\right) - b\epsilon^\alpha \rho^\alpha \mathbf{g} - \sum_{\kappa\in\mathcal{I}_{c\alpha}} b\langle \mathbf{t}_\alpha\cdot\mathbf{n}_\alpha\rangle_{\Omega_\kappa,\Omega} \\ &\qquad + \sum_{\text{ends}} b\left\langle\left[\rho_\alpha\left(\mathbf{v}_\alpha - \mathbf{v}^{\overline{\alpha}}\right)(\mathbf{v}_\alpha - \mathbf{w}_{\text{end}}) - \mathbf{t}_\alpha\right]\cdot\mathbf{n}_\alpha\right\rangle_{\Omega_{\alpha_{\text{end}}},\Omega} = 0. \end{aligned} \tag{25}$$

In modeling porous media, it is common to assume the flow is slow enough that the advection terms and the time derivative in the momentum equation are negligible. The advection terms are considered small because they involve velocity squared, which is small when the velocity is small. These assumptions of small terms need not be made to continue the derivation. However, because we will be assuming that the flow is slow, the derivation is simplified if we impose this constraint at this time and also drop the momentum flux expressions at the top and bottom of the region as well as the other terms involving products of velocity. Thus eqn (25) reduces to

$$-\nabla'\cdot\left(b\epsilon^\alpha \mathbf{t}^{\overline{\overline{\alpha}}\prime}\right) - b\epsilon^\alpha \rho^\alpha \mathbf{g} - \sum_{\kappa\in\mathcal{I}_{c\alpha}} b\langle \mathbf{t}_\alpha\cdot\mathbf{n}_\alpha\rangle_{\Omega_\kappa,\Omega} - \sum_{\text{ends}} b\langle \mathbf{t}_\alpha\cdot\mathbf{n}_\alpha\rangle_{\Omega_{\alpha_{\text{end}}},\Omega} = 0, \tag{26}$$

and eqn (23) simplifies to

$$\epsilon^{\alpha}\mathbf{t}^{\overline{\overline{\alpha}}\prime} = (\mathbf{I} - \mathbf{\Lambda}\mathbf{\Lambda})\cdot\langle\mathbf{t}_{\alpha}\rangle_{\Omega_{\alpha},\Omega}. \tag{27}$$

Finally, we will make use of the standard constitutive form for the microscale stress tensor for a Newtonian fluid such that

$$\mathbf{t}_{\alpha} = -p_{\alpha}\mathbf{I} + \boldsymbol{\tau}_{\alpha}. \tag{28}$$

Thus, eqn (26) becomes

(29)
$$\nabla'\left(b\epsilon^{\alpha}p^{\alpha}\right) - \nabla'\cdot\left(b\epsilon^{\alpha}\boldsymbol{\tau}^{\overline{\overline{\alpha}}\prime}\right) - b\epsilon^{\alpha}\rho^{\alpha}\mathbf{g} + \sum_{\kappa\in\mathcal{J}_{c\alpha}} b\langle p_{\alpha}\mathbf{n}_{\alpha}\rangle_{\Omega_{\kappa},\Omega} - \sum_{\kappa\in\mathcal{J}_{c\alpha}} b\langle\boldsymbol{\tau}_{\alpha}\cdot\mathbf{n}_{\alpha}\rangle_{\Omega_{\kappa},\Omega} + \sum_{\text{ends}} b\langle p_{\alpha}\mathbf{n}_{\alpha}\rangle_{\Omega_{\alpha_{\text{end}}},\Omega} - \sum_{\text{ends}} b\langle\boldsymbol{\tau}_{\alpha}\cdot\mathbf{n}_{\alpha}\rangle_{\Omega_{\alpha_{\text{end}}},\Omega} = 0.$$

We assume that the viscous effects within the fluid are small in comparison to viscous interactions between phases (e.g., of the fluid with the solid). Therefore, intra-fluid viscous terms are neglected so that eqn (29) simplifies further to

$$\nabla'\left(b\epsilon^{\alpha}p^{\alpha}\right) - b\epsilon^{\alpha}\rho^{\alpha}\mathbf{g} + \sum_{\kappa\in\mathcal{J}_{c\alpha}} b\langle p_{\alpha}\mathbf{n}_{\alpha}\rangle_{\Omega_{\kappa},\Omega} - \sum_{\kappa\in\mathcal{J}_{c\alpha}} b\langle\boldsymbol{\tau}_{\alpha}\cdot\mathbf{n}_{\alpha}\rangle_{\Omega_{\kappa},\Omega} + \sum_{\text{ends}} b\langle p_{\alpha}\mathbf{n}_{\alpha}\rangle_{\Omega_{\alpha_{\text{end}}},\Omega} = 0. \tag{30}$$

Although it has been averaged to the megascale over the direction normal to the bottom of the region of interest, momentum eqn (30) is still a three-dimensional vector equation. Despite the fact that the averaging direction is not truly vertical, unless the dip angle $\theta = 0$, we will refer to the process of eliminating accounting for gradients in the direction normal to the bottom surface as vertical averaging. We can obtain the vertical component of the momentum equation by taking the dot product of eqn (30) with $\mathbf{\Lambda}$ and the lateral vector component by taking the dot product with $\mathbf{I} - \mathbf{\Lambda}\mathbf{\Lambda}$. We will find these in turn.

2.6. Vertical Component of the Momentum Equation. When taking the dot product of eqn (30) with $\mathbf{\Lambda}$ while noting that, in this formulation, $\mathbf{\Lambda}$ is a constant that can be moved inside the averaging operator, we obtain

$$-b\epsilon^{\alpha}\rho^{\alpha}\mathbf{g}\cdot\mathbf{\Lambda} + \sum_{\kappa\in\mathcal{J}_{c\alpha}} b\langle p_{\alpha}\mathbf{n}_{\alpha}\cdot\mathbf{\Lambda}\rangle_{\Omega_{\kappa},\Omega} - \sum_{\kappa\in\mathcal{J}_{c\alpha}} b\mathbf{\Lambda}\cdot\langle\boldsymbol{\tau}_{\alpha}\cdot\mathbf{n}_{\alpha}\rangle_{\Omega_{\kappa},\Omega} + \sum_{\text{ends}} b\langle p_{\alpha}\mathbf{n}_{\alpha}\cdot\mathbf{\Lambda}\rangle_{\Omega_{\alpha_{\text{end}}},\Omega} = 0. \tag{31}$$

For the system of interest here, the volume fraction of a phase is constant in each section considered. Additionally, the pressure over each end of the averaging region is approximately constant so that we can integrate the last term on the left side of eqn (31) to obtain

$$-b\epsilon^{\alpha}\rho^{\alpha}\mathbf{g}\cdot\mathbf{\Lambda} + \sum_{\kappa\in\mathcal{J}_{c\alpha}} b\langle p_{\alpha}\mathbf{n}_{\alpha}\cdot\mathbf{\Lambda}\rangle_{\Omega_{\kappa},\Omega} - \sum_{\kappa\in\mathcal{J}_{c\alpha}} b\mathbf{\Lambda}\cdot\langle\boldsymbol{\tau}_{\alpha}\cdot\mathbf{n}_{\alpha}\rangle_{\Omega_{\kappa},\Omega} + \epsilon^{\alpha}p_{\alpha\text{top}} - \epsilon^{\alpha}p_{\alpha\text{bot}} = 0. \tag{32}$$

We will make use of eqn (32) for the w and n phases only in sections where these phases are continuous and mobile. Because the volume fraction is constant in each

region, the first summation in eqn (32) will be negligible. Then division by ϵ^α and rearrangement of the equation yields

$$-b\rho^\alpha \mathbf{g}\cdot\mathbf{\Lambda} + p_{\alpha\text{top}} - p_{\alpha\text{bot}} = \sum_{\kappa\in\mathcal{I}_{c\alpha}} \frac{b}{\epsilon^\alpha}\mathbf{\Lambda}\cdot\langle\boldsymbol{\tau}_\alpha\cdot\mathbf{n}_\alpha\rangle_{\Omega_\kappa,\Omega}. \tag{33}$$

The term on the right side will be zero at equilibrium, i.e. when $\mathbf{q}^{\overline{\overline{\alpha}}} = 0$. Thus we can make a Taylor series expansion of this term around this equilibrium state to obtain an expression of the form

$$\sum_{\kappa\in\mathcal{I}_{c\alpha}} \langle\boldsymbol{\tau}_\alpha\cdot\mathbf{n}_\alpha\rangle_{\Omega_\kappa,\Omega} = -\epsilon^\alpha\hat{\mu}^\alpha\hat{\mathbf{R}}^\alpha\cdot\mathbf{q}^{\overline{\overline{\alpha}}}, \tag{34}$$

where $\hat{\mathbf{R}}^\alpha$ is a resistance tensor. Substitution of eqn (34) into eqn (33) then provides

$$-b\rho^\alpha \mathbf{g}\cdot\mathbf{\Lambda} + p_{\alpha\text{top}} - p_{\alpha\text{bot}} = -b\hat{\mu}^\alpha\mathbf{\Lambda}\cdot\hat{\mathbf{R}}^\alpha\cdot\mathbf{q}^{\overline{\overline{\alpha}}}. \tag{35}$$

This equation describes vertical flow of an α phase fluid in a vertically megascopic domain where the volume fraction is constant.

It has been shown that the applicable condition between two phases at a larger scale interface (i.e., at an interface between regions in Fig 1) where there is a discontinuous change in volume fraction is that the pressure is continuous [27]. Making use of this condition, we can apply eqn (35) for a w phase that is mobile over regions 1 and 2 of the current problem, as described in Table 1, by adding the equations for the two regions. The result is

$$-h\rho^w \mathbf{g}\cdot\mathbf{\Lambda} + p_{wh} - p_{w0} = -\hat{\mu}^w\mathbf{\Lambda}\cdot\left[h_i\hat{\mathbf{R}}_1^w\cdot\mathbf{q}_1^{\overline{\overline{w}}} + (h-h_i)\,\hat{\mathbf{R}}_2^w\cdot\mathbf{q}_2^{\overline{\overline{w}}}\right]. \tag{36}$$

The n phase is mobile only in region 3, so its vertical momentum equation is

$$-(H-h)\,\rho^n \mathbf{g}\cdot\mathbf{\Lambda} + p_{nH} - p_{nh} = -\hat{\mu}^n\,(H-h)\,\mathbf{\Lambda}\cdot\hat{\mathbf{R}}_3^n\cdot\mathbf{q}_3^{\overline{\overline{n}}}. \tag{37}$$

For each phase, if the resistance tensor $\hat{\mathbf{R}}^\alpha$ aligns with the coordinate system such that it has only diagonal components (a condition that includes the case of an isotropic medium) and the vertical flow is negligible, the hydrostatic conditions for each phase are obtained, respectively, as

$$-h\rho^w \mathbf{g}\cdot\mathbf{\Lambda} + p_{wh} - p_{w0} = 0, \tag{38}$$

and

$$-(H-h)\,\rho^n \mathbf{g}\cdot\mathbf{\Lambda} + p_{nH} - p_{nh} = 0. \tag{39}$$

It is interesting to note that for an anisotropic region in which the coordinate axes do not align with the principal direction of the resistance tensor such that off-diagonal elements of $\hat{\mathbf{R}}^\alpha$ are non-zero, a deviation from these hydrostatic conditions can occur due to the lateral flow.

2.7. Lateral Component of the Momentum Equation. We can take the dot product of eqn (30) with the tensor $\mathbf{I}' = \mathbf{I} - \mathbf{\Lambda}\mathbf{\Lambda}$ to obtain the momentum equation in the directions tangent to the bottom of the study region. Since $\mathbf{\Lambda}$ is a constant, $\mathbf{I}'$ can be moved inside the averaging operator if desired. Thus, we obtain

$$\begin{aligned}\nabla'(b\epsilon^\alpha p^\alpha) - b\epsilon^\alpha\rho^\alpha\mathbf{g}\cdot\mathbf{I}' + \sum_{\kappa\in\mathcal{I}_{c\alpha}} b\mathbf{I}'\cdot\langle p_\alpha\mathbf{n}_\alpha\rangle_{\Omega_\kappa,\Omega} \\ - \sum_{\kappa\in\mathcal{I}_{c\alpha}} b\mathbf{I}'\cdot\langle\boldsymbol{\tau}_\alpha\cdot\mathbf{n}_\alpha\rangle_{\Omega_\kappa,\Omega} + \sum_{\text{ends}} b\mathbf{I}'\cdot\langle p_\alpha\mathbf{n}_\alpha\rangle_{\Omega_{\alpha_{\text{end}}},\Omega} = 0.\end{aligned} \tag{40}$$

We can apply the product rule to the lateral gradient term and eliminate $\nabla'(b\epsilon^\alpha)$ using eqn (77) to obtain

$$\begin{aligned} b\epsilon^\alpha \nabla' p^\alpha - b\epsilon^\alpha \rho^\alpha \mathbf{g}\cdot\mathbf{l}' + \sum_{\kappa\in\mathcal{J}_{c\alpha}} b\mathbf{l}'\cdot\langle (p_\alpha - p^\alpha)\,\mathbf{n}_\alpha\rangle_{\Omega_\kappa,\Omega} \\ - \sum_{\kappa\in\mathcal{J}_{c\alpha}} b\mathbf{l}'\cdot\langle \boldsymbol{\tau}_\alpha\cdot\mathbf{n}_\alpha\rangle_{\Omega_\kappa,\Omega} + \sum_{\text{ends}} b\mathbf{l}'\cdot\langle (p_\alpha - p^\alpha)\,\mathbf{n}_\alpha\rangle_{\Omega_{\alpha_{\text{end}}},\Omega} = 0. \end{aligned} \tag{41}$$

Make use of constitutive eqn (34) to relate the frictional interactions between phases. Subsequent rearrangement of terms yields

$$\begin{aligned} b\hat{\mu}^\alpha \mathbf{l}'\cdot\hat{\mathbf{R}}^\alpha\cdot\mathbf{q}^{\overline{\overline{\alpha}}} = -\,b\left(\nabla' p^\alpha - \rho^\alpha \mathbf{g}\cdot\mathbf{l}'\right) - \sum_{\kappa\in\mathcal{J}_{c\alpha}} \frac{b}{\epsilon^\alpha}\mathbf{l}'\cdot\langle (p_\alpha - p^\alpha)\,\mathbf{n}_\alpha\rangle_{\Omega_\kappa,\Omega} \\ - \sum_{\text{ends}} \frac{b}{\epsilon^\alpha}\mathbf{l}'\cdot\langle (p_\alpha - p^\alpha)\,\mathbf{n}_\alpha\rangle_{\Omega_{\alpha_{\text{end}}},\Omega}. \end{aligned} \tag{42}$$

We will consider the hydrostatic case where the vertical flow is considered negligible. For this case, we can set

$$\mathbf{q}^{\overline{\overline{\alpha}}} = \mathbf{l}'\cdot\mathbf{q}^{\overline{\overline{\alpha}}} = \mathbf{l}'\cdot\mathbf{q}^{\overline{\overline{\alpha}}\prime}. \tag{43}$$

Then we can also define the lateral direction resistance tensor according to

$$\hat{\mathbf{R}}^{\alpha\prime\prime} = \mathbf{l}'\cdot\hat{\mathbf{R}}^\alpha\cdot\mathbf{l}', \tag{44}$$

and its inverse as

$$\hat{\mathbf{K}}^{\alpha\prime\prime} = \left(\hat{\mathbf{R}}^{\alpha\prime\prime}\right)^{-1}. \tag{45}$$

These last three identities allow eqn (42) to be expressed as

$$\begin{aligned} b\mathbf{q}^{\overline{\overline{\alpha}}\prime} = -\,b\frac{\hat{\mathbf{K}}^{\alpha\prime\prime}}{\hat{\mu}^\alpha}\cdot\left(\nabla' p^\alpha - \rho^\alpha \mathbf{g}\cdot\mathbf{l}'\right) - \sum_{\kappa\in\mathcal{J}_{c\alpha}} \frac{b}{\epsilon^\alpha}\frac{\hat{\mathbf{K}}^{\alpha\prime\prime}}{\hat{\mu}^\alpha}\cdot\langle (p_\alpha - p^\alpha)\,\mathbf{n}_\alpha\rangle_{\Omega_\kappa,\Omega} \\ - \sum_{\text{ends}} \frac{b}{\epsilon^\alpha}\frac{\hat{\mathbf{K}}^{\alpha\prime\prime}}{\hat{\mu}^\alpha}\cdot\langle (p_\alpha - p^\alpha)\,\mathbf{n}_\alpha\rangle_{\Omega_{\alpha_{\text{end}}},\Omega}. \end{aligned} \tag{46}$$

For the case where the volume fraction within the region is a constant, the first summation on the right side will be negligible so that the final form of the lateral momentum equation simplifies further to

$$b\mathbf{q}^{\overline{\overline{\alpha}}\prime} = -b\frac{\hat{\mathbf{K}}^{\alpha\prime\prime}}{\hat{\mu}^\alpha}\cdot\left(\nabla' p^\alpha - \rho^\alpha \mathbf{g}\cdot\mathbf{l}'\right) - \sum_{\text{ends}} \frac{b}{\epsilon^\alpha}\frac{\hat{\mathbf{K}}^{\alpha\prime\prime}}{\hat{\mu}^\alpha}\cdot\langle (p_\alpha - p^\alpha)\,\mathbf{n}_\alpha\rangle_{\Omega_{\alpha_{\text{end}}},\Omega}. \tag{47}$$

The integrals over the ends of the domain can also be evaluated directly making use of the fact that the variation of the pressure over an end of the averaging volume is negligible. At the top of the region, we have

$$\frac{b}{\epsilon^\alpha}\frac{\hat{\mathbf{K}}^{\alpha\prime\prime}}{\hat{\mu}^\alpha}\cdot\langle (p_\alpha - p^\alpha)\,\mathbf{n}_\alpha\rangle_{\Omega_{\alpha_{\text{top}}},\Omega} = -\frac{\hat{\mathbf{K}}^{\alpha\prime\prime}}{\hat{\mu}^\alpha}\cdot\left(p_{\alpha\text{top}} - p^\alpha\right)\nabla' z_{\text{top}}, \tag{48}$$

while at the bottom,

$$\frac{b}{\epsilon^\alpha}\frac{\hat{\mathbf{K}}^{\alpha\prime\prime}}{\hat{\mu}^\alpha}\cdot\langle (p_\alpha - p^\alpha)\,\mathbf{n}_\alpha\rangle_{\Omega_{\alpha_{\text{bot}}},\Omega} = \frac{\hat{\mathbf{K}}^{\alpha\prime\prime}}{\hat{\mu}^\alpha}\cdot\left(p_{\alpha\text{bot}} - p^\alpha\right)\nabla' z_{\text{bot}}. \tag{49}$$

Therefore

(50)
$$\sum_{\text{ends}} \frac{b}{\epsilon^\alpha} \frac{\hat{\mathbf{K}}^{\alpha}{}''}{\hat{\mu}^\alpha} \cdot \langle (p_\alpha - p^\alpha)\, \mathbf{n}_\alpha \rangle_{\Omega_{\alpha_{\text{end}}},\Omega} = -\frac{\hat{\mathbf{K}}^{\alpha}{}''}{\hat{\mu}^\alpha} \cdot \left(p_{\alpha\text{top}} \nabla' z_{\text{top}} - p_{\alpha\text{bot}} \nabla' z_{\text{bot}} - p^\alpha \nabla' b\right).$$

Substitution of this expression into eqn (47) gives the form of the lateral momentum equation for a region as

(51)
$$b\mathbf{q}^{\overline{\overline{\alpha}}\prime} = -b\frac{\hat{\mathbf{K}}^{\alpha}{}''}{\hat{\mu}^\alpha} \cdot \left(\nabla' p^\alpha - \rho^\alpha \mathbf{g}\cdot\mathbf{l}'\right) + \frac{\hat{\mathbf{K}}^{\alpha}{}''}{\hat{\mu}^\alpha} \cdot \left(p_{\alpha\text{top}} \nabla' z_{\text{top}} - p_{\alpha\text{bot}} \nabla' z_{\text{bot}} - p^\alpha \nabla' b\right).$$

From Table 1, we know that the wetting phase is mobile only in regions 1 and 2. Therefore, we can apply eqn (51) to these two regions and add the results to obtain the lateral momentum equation for phase w in any cross section. The result is

(52)
$$\begin{aligned} h_i \mathbf{q}_1^{\overline{\overline{w}}\prime} + (h - h_i)\mathbf{q}_2^{\overline{\overline{w}}\prime} &= -h_i \frac{\hat{\mathbf{K}}_1^{w}{}''}{\hat{\mu}^w} \cdot \left(\nabla' p_1^w - \rho^w \mathbf{g}\cdot\mathbf{l}'\right) \\ &\quad - (h - h_i)\frac{\hat{\mathbf{K}}_2^{w}{}''}{\hat{\mu}^w} \cdot \left(\nabla' p_2^w - \rho^w \mathbf{g}\cdot\mathbf{l}'\right) + \frac{\hat{\mathbf{K}}_1^{w}{}''}{\hat{\mu}^w} \cdot \left(p_{wh_i} \nabla' h_i - p_1^w \nabla' h_i\right) \\ &\quad + \frac{\hat{\mathbf{K}}_2^{w}{}''}{\hat{\mu}^w} \cdot \left[p_{wh} \nabla' h - p_{wh_i} \nabla' h_i - p_2^w \nabla' (h - h_i)\right]. \end{aligned}$$

Now note that all the pressures appearing in eqn (52) can be expressed in terms of p_{wh} since the vertical pressure gradient is hydrostatic. These expressions are

(53)
$$p_1^w = p_{wh_i} - \frac{1}{2} h_i \rho^w \mathbf{g}\cdot\mathbf{\Lambda},$$

(54)
$$p_2^w = p_{wh_i} + \frac{1}{2}(h - h_i)\rho^w \mathbf{g}\cdot\mathbf{\Lambda},$$

and

(55)
$$p_{wh} = p_{wh_i} + (h - h_i)\rho^w \mathbf{g}\cdot\mathbf{\Lambda}.$$

Substitution of these three expressions into eqn (52) and collection of terms then provides

(56)
$$h_i \mathbf{q}_1^{\overline{\overline{w}}\prime} + (h - h_i)\mathbf{q}_2^{\overline{\overline{w}}\prime} = -\left[h_i \frac{\hat{\mathbf{K}}_1^{w}{}''}{\hat{\mu}^w} + (h - h_i)\frac{\hat{\mathbf{K}}_2^{w}{}''}{\hat{\mu}^w}\right] \cdot \left(\nabla' p_{wh} - \rho^w \mathbf{g}\cdot\mathbf{\Lambda}\nabla' h - \rho^w \mathbf{g}\cdot\mathbf{l}'\right).$$

In terms of relative permeabilities for each region, the permeability in each section may be denoted as

(57)
$$\hat{\mathbf{K}}_1^{w}{}'' = \hat{\mathbf{K}}''\cdot\hat{\mathbf{k}}_{1\text{rel}}^{w}{}'',$$

and

(58)
$$\hat{\mathbf{K}}_2^{w}{}'' = \hat{\mathbf{K}}''\cdot\hat{\mathbf{k}}_{2\text{rel}}^{w}{}''.$$

Therefore, we can define the effective relative permeability for the wetting phase over the full height of the study system, $\hat{\mathbf{k}}_{r\text{eff}}^{w}{}''$, as

(59)
$$\hat{\mathbf{k}}_{r\text{eff}}^{w}{}'' = \frac{h_i \hat{\mathbf{k}}_{1\text{rel}}^{w}{}'' + (h - h_i)\hat{\mathbf{k}}_{2\text{rel}}^{w}{}''}{H}.$$

Substitution of this definition and the definition of eqn (14) into eqn (56) gives

$$H\mathbf{Q}^{\overline{\overline{w}}\prime} = -H\frac{\hat{\mathbf{K}}''}{\hat{\mu}^w}\cdot\hat{\mathbf{k}}_{r\mathrm{eff}}^{\,w}{}''\cdot\left(\nabla' p_{wh} - \rho^w \mathbf{g}\cdot\mathbf{\Lambda}\nabla' h - \rho^w \mathbf{g}\cdot\mathbf{I}'\right). \tag{60}$$

Table 1 indicates that the non-wetting phase is mobile only in region 3. Therefore, eqn (51) may be applied to this region to obtain the lateral momentum equation for phase n in any cross section. The result is

$$\begin{aligned}(H-h)\,\mathbf{q}_3^{\overline{\overline{n}}\prime} = &-(H-h)\,\frac{\hat{\mathbf{K}}_3^{n}{}''}{\hat{\mu}^n}\cdot\left(\nabla' p_3^n - \rho^n \mathbf{g}\cdot\mathbf{I}'\right)\\ &+\frac{\hat{\mathbf{K}}_3^{n}{}''}{\hat{\mu}^n}\cdot\left[p_{nH}\nabla' H - p_{nh}\nabla' h - p_3^n\nabla'(H-h)\right].\end{aligned} \tag{61}$$

The pressures appearing in eqn (61) can be expressed in terms of p_{nh} since the vertical pressure gradient is hydrostatic. These expressions are:

$$p_3^n = p_{nh} + \frac{1}{2}(H-h)\,\rho^n \mathbf{g}\cdot\mathbf{\Lambda}, \tag{62}$$

and

$$p_{nh} = p_{nH} - (H-h)\,\rho^n \mathbf{g}\cdot\mathbf{\Lambda}. \tag{63}$$

Substitution of these relations into eqn (61) and collection of terms then provides

$$(H-h)\,\mathbf{q}_3^{\overline{\overline{n}}\prime} = -(H-h)\,\frac{\hat{\mathbf{K}}_3^{n}{}''}{\hat{\mu}^n}\cdot\left(\nabla' p_{nh} - \rho^n \mathbf{g}\cdot\mathbf{\Lambda}\nabla' h - \rho^n \mathbf{g}\cdot\mathbf{I}'\right). \tag{64}$$

The relative permeability may be denoted as

$$\hat{\mathbf{K}}_3^{n}{}'' = \hat{\mathbf{K}}''\cdot\hat{\mathbf{k}}_{3\mathrm{rel}}^{\,n}{}''. \tag{65}$$

Therefore, we can define the effective relative permeability for the non-wetting phase over the full height of the study system, $\hat{\mathbf{k}}_{r\mathrm{eff}}^{\,n}{}''$, as

$$\hat{\mathbf{k}}_{r\mathrm{eff}}^{\,n}{}'' = (H-h)\,\hat{\mathbf{k}}_{3\mathrm{rel}}^{\,n}{}''. \tag{66}$$

Substitution of this definition and the definition of eqn (14) into eqn (64) gives

$$H\mathbf{Q}^{\overline{\overline{n}}\prime} = -H\frac{\hat{\mathbf{K}}''}{\hat{\mu}^n}\cdot\hat{\mathbf{k}}_{r\mathrm{eff}}^{\,n}{}''\cdot\left(\nabla' p_{nh} - \rho^n \mathbf{g}\cdot\mathbf{\Lambda}\nabla' h - \rho^n \mathbf{g}\cdot\mathbf{I}'\right). \tag{67}$$

Simulation of CO_2 migration based on equations obtained from megascale averaging in the vertical and macroscale averaging in the lateral directions involves simultaneous solution of mass balance eqn (17) with $\alpha = \{w, n\}$ and hysteresis model eqn (19) with the phase momentum equations given by eqns (60) and (67).

3. Numerical simulations

We applied the VE model presented above to CO_2 migration within several saline aquifer systems composed of varying caprock topography. The simulations were designed to meet two objectives: 1) to verify the VE model against a fully three-dimensional simulator and 2) to examine the effect of caprock topography on long-term CO_2 migration. The VE model equations are solved using the ECLIPSE reservoir simulator, which can be run using a VE option (ECL-VE) [54]. Specifically, we used ECLIPSE 100 which is based on a black-oil formulation of the multiphase flow equations. For model verification, the three-dimensional simulations were performed using the standard 3D option (ECL-3D) [54].

To capture the effect of caprock topography, a number of different aquifer geometries were simulated using the ECL-VE and ECL-3D models. These simulations

were performed on two types of domains: two-dimensional vertical cross-sections as well as three-dimensional domains. The natural undulations of a typical caprock surface are represented by sinusoidal functions that are superimposed on a sloping caprock. The roughness of the surface, which refers to the extent of variation in the topography, is captured by adjusting the amplitude and frequency of the underlying function. Although these geometries are idealizations of real systems, they can provide needed insight into the effects of caprock topography on plume migration.

In addition to the ECLIPSE simulations, each of the two-dimensional scenarios was also simulated with a research code based on the VE formulation (VESA) [22]. Preliminary comparisons indicated that, for practical purposes, solutions computed with ECL-VE and VESA are identical for all scenarios. Thus, for the sake of brevity, the discussion focuses primarily on the ECL-VE simulator results with VESA results considered only in a few cases. However, we do emphasize that the comparison between both VE simulators allows us to verify their implementations of the vertically averaged equations derived in the previous section.

3.1. Setup. In the simulations we consider a sloping aquifer with mean thickness H_0. To evaluate the effect of an irregular aquifer geometry we introduce a fluctuation in the elevation of the top of the aquifer that we model by a sinusoidal series such that caprock position is given by

$$H(x,y) = H_0 + H_0 \left[\sum_{i=0}^{N_x} a_i^x cos(k_i^x x + \gamma_i^x) + \sum_{i=0}^{N_y} a_i^y cos(k_i^y y + \gamma_i^y) \right], \tag{68}$$

where k_i^x and k_i^y are the wavenumbers of the i-th sinusoidal perturbation in the x and y directions, a_i^x and a_i^y are relative amplitudes with respect to the mean aquifer thickness, and γ_i^x and γ_i^y are phase shift angles. The wavenumber is computed as $k_i = n_i 2\pi/L$, where L is the length of aquifer in the respective direction, hence n_i is the number of periods of the perturbation within the aquifer length L.

In all the simulations, the linear relative permeability curves shown in Fig 2 are used. To include the effect of residual trapping, we selected the end points of the curves such that they correspond to residual saturation values measured in laboratory experiments [3]. Capillary forces were neglected to be consistent with the derivation of the VE equations presented above for a sharp interface model. Values selected for other fluid properties, such as density and viscosity, are those reported in other studies that simulated CO_2 migration in large scale domains [14] and are summarized in Table 2.

3.2. Two-dimensional application. We first present simulations that consider CO_2 migration along a two-dimensional vertical cross-section of an aquifer. Table 3 summarizes the parameters that define the aquifer and grid geometries for this set of problems. In this set of simulations, the mean direction of the aquifer forms an angle θ with the x axis. Boundary conditions specify no-flow through the top, bottom and left sides of the domain while a constant hydrostatic pressure is applied at the right boundary of the domain. We generated sixteen different aquifer geometries assuming a single sinusoidal perturbation with four different values of the relative amplitude $a_0^x = [0.05, 0.10, 0.15, 0.20]$ and four different number of periods $n_0^x = [10, 20, 40, 80]$. In addition, a base case was simulated that considers a flat aquifer.

3.2.1. Comparison of VE and 3D solutions. Figs 3 and 4 provide comparisons of simulated CO_2 migration using the ECL-VE and ECL-3D models for two of the

cross-section geometries. These two scenarios represent the range in amplitudes examined. The amplitude factor used in Fig 3, $a = 0.05$ is 1/4 of that used in Fig 4; but both figures use the same value of frequency, $n_0^x = 40$.

In Fig 3, we observe that the two solutions agree well for the smallest amplitude case. In general, the VE solution for the mobile CO_2 region matches the location of the 3D interface over the extent of the plume. The slight separation between the solutions is caused by the vertical discretization used in the 3D simulation, which does not match the flat contours of saturation of the CO_2 that has collected beneath the domes of the caprock topography. The orientation of the vertical cells leads to an unrealistic jagged CO_2 interface. The plume tip for the VE solution also extends farther ahead of the 3D solution at late time (1300 years), however this difference is also likely attributed to discretization and other numerical artifacts of both the VE and 3D simulations.

The model comparison for the second geometry (Fig 4) is qualitatively similar to the smaller amplitude geometry discussed above. Along the trailing edge of the mobile interface, and where the CO_2 has collected in the caprock domes, the solutions are nearly identical. However, the differences at the plume tip after 1300 years are greater for this case than observed in Fig 3c. This larger discrepancy is expected for a perturbation with larger amplitude because, as the caprock elevation changes more abruptly, the ability to capture the migration on the left edge of each dome (spill points) becomes increasingly difficult. This is particularly true for the 3D model because of the more irregular numerical grid that must be used to sufficiently discretize the rapidly changing caprock surface.

It is useful to compare the solution of the VE-based simulators, ECL-VE and VESA, to better understand the behavior of VE models for the systems studied here. Fig 5 shows a comparison of the interfaces of the mobile CO_2 region after 1300 years estimated by the two simulators. The solutions are identical over the entire extent of the CO_2 plume. Based on the agreement between the VE solvers, we believe that differences of these solutions with those of the three-dimensional ECL-3D simulation are most likely due to the limited vertical resolution of the latter, which is particularly important to capture abrupt changes in the caprock elevation, as discussed above.

3.2.2. Plume speed and migration distance. Fig 6 shows CO_2 saturation after 100 and 1300 years for three aquifer configurations. In all cases, we observe that initially the plume spreads laterally from the source zone, with the upslope and downslope edges moving almost equal distances in both directions. Then as buoyancy forces become more dominant, the entire plume migrates along the caprock boundary in the dip direction. For the cases with varying caprock geometry, the leading edge of the plume follows the contours of the caprock, filling successive domes as it progresses updip. At the trailing edge, the CO_2 becomes immobilized by the topography, in the varying geometry cases. In all cases, some portion of the CO_2 is trapped in the residual phase, but the relative amount decreases with higher values of amplitude.

It is clear from comparing the simulations with different sinusoidal amplitudes that CO_2 migrates more slowly as the amplitude of the irregularity increases. On the other hand, the amount of structurally trapped CO_2 increases with the amplitude of the caprock height variability. Note that CO_2 is only trapped due to residual trapping (light blue areas) in the flat aquifer case, and most of the initial volume is still mobile after 1300 years. However, for the aquifer with $a_0^x = 0.15$, all the initial CO_2 volume is completely trapped either by residual trapping or in

structurally trapped pools beneath the irregular caprock surface. The volume of the aquifer that is available for structural CO_2 trapping is given by the space between the top of the aquifer and horizontal lines that are tangent to the caprock surface at adjacent (upslope) local minimum points.

Figs 7 and 8 show the position of the plume tip simulated with ECL-VE versus time as function of the relative amplitude and number of periods of the caprock oscillations, respectively. Fig 7 shows that caprocks with higher frequencies results in slower migration speeds. As the oscillation frequency increases from zero for a flat aquifer to higher values of n_0^x for a given amplitude, the curves that describe the tip position versus time appear to converge to a unique curve, hereafter referred to as the effective curve, as the number of periods approaches infinity. While the difference between the flat aquifer and the effective curves does depend on the oscillation amplitude, the convergence rate of the curves towards the effective one is independent of the magnitude of the fluctuation. For example, the difference between the curves that correspond to $n_0^x = 40$ and $n_0^x = 80$ is similar for all the amplitudes considered. This means that oscillations with higher frequencies would not result in additional reductions of the plume migration speed.

Fig 8 shows that CO_2 advances slower for larger oscillation amplitudes. Moreover, as the amplitude becomes larger the volume of CO_2 that is trapped beneath the aquifer caprock increases. For some of the simulations the initial CO_2 volume has been completely trapped before the end of the simulated period so that the plume tip remains at the same position (curves for $a_0^x = 0.15$ and $a_0^x = 0.2$ in Figs 8c and 8d). In these cases, we observe that the final migration distance is similar for all caprocks with the same amplitude. For example, we observe in Fig 7d that the maximum distance traveled is between 4 and 5 km from the injection point for all frequencies of the case with amplitude $a_0^x = 0.2$. The difference in these four cases can be related to the difference in distance traveled by CO_2 collected in one individual period for a low frequency case (i.e. $n_0^x = 10$) versus several individual periods for a higher frequency case (i.e. $n_0^x = 80$).

The effect of amplitude on the upslope velocity, amount of CO_2 trapped by the topography, and maximum distance traveled is consistent with the use of a sinusoidal function to represent an irregular caprock. This relationship is expected because the total volume of CO_2 that can be trapped per unit length of aquifer only depends on the amplitude of the oscillation and not its frequency. Furthermore, in contrast to the convergent behavior of the curves in Fig 7, there is no evidence of convergence with respect to amplitude, as indicated by the constant separation between curves that correspond to different amplitudes in Fig 8. Hence, the reduction in the plume migration speed due to increasing amplitudes does not have a limit, and one can expect that larger oscillations will result in even lower plume speed and shorter migration distances due to larger trapped CO_2 volume.

3.3. Three-dimensional application. It is reasonable to expect that the effects of caprock topography on the plume speed and migration distance observed in the two-dimensional cross sections presented above also occur in three-dimensional scenarios. This was the main motivation to set up an additional set of simulations that considers fully three-dimensional aquifers. The parameters used to define the grid and aquifer geometries and the initial plume are listed in Table 4. For the ECL-3D simulations, the cell size and dimensions of the domain result in a numerical grid that has 300 x 300 x 50 cells, which correspond to a 4.5 million cells grid. The ECL-VE simulations solve the same system on a 300 x 300 grid, or a total of 90,000 cells.

The large dimensions of the 3D grid result in much longer run times for ECL-3D than for the 2D cross-section simulations, thus we only consider two 3D aquifers: i) an aquifer with flat caprock, and ii) an aquifer with irregular caprock generated by the superposition of sinusoidal perturbations in the x and y directions. This three-dimensional domain is also simulated using the ECL-VE model for comparison. The sinusoidal functions were generated assuming that ten wave periods fit in the domain in each direction and with relative amplitudes of $a_x = a_y = a = 0.05$. The dip direction of the aquifers forms a 0.286° angle (0.5% slope) with the x axis.

The ECL-VE and ECL-3D models compared well for the three-dimensional aquifers, and therefore only the ECL-VE results will be reported here. To view the ECL-VE results more effectively, 3D CO_2 saturations are reconstructed from the VE solution for the mobile and residual CO_2 interfaces and then projected onto a 3D image. To produce the needed data set, saturation values are assigned to each cell in the three-dimensional grid according to the value of the calculated CO_2 thickness for the corresponding grid columns. Thus, reconstructed saturation values in cells that intersect the VE solution for the CO_2-brine interface have a value smaller than 1, which is due to the irregular vertical grid spacing of the 3D grid.

Fig 9 shows a top view of reconstructed CO_2 saturation values from the ECL-VE simulations. This figure shows the simulated CO_2 plumes after 1000 years. While saturation contours are smooth and continuous for the flat aquifer, they are discontinuous and irregular for the case of varying caprock geometry. This occurs because of the of CO_2 pools that accumulate in the local dome features of the caprock topography. It is clear that the plume moves slower in the aquifer with sinusoidal caprock than in the flat aquifer, by about 50%. At the end of the simulated time, the CO_2 in the irregular caprock case is completely trapped by structural features or in the residual phase, whereas the majority of CO_2 in the flat caprock case remains mobile.

Fig 10 shows reconstructed CO_2 saturation values along two vertical cross-sections of the 3D domain. The accumulation of CO_2 beneath the irregular caprock is evident in this figure. This figure also shows the greater extent of plume spreading from the initial square condition for the flat caprock case. This result implies not only enhanced structural trapping obtained by an irregular caprock, but also a reduction in the plume footprint caused by the caprock roughness. Projected plume footprint may potentially be an important factor in consideration of potential CO_2 storage sites.

4. Conclusions

This manuscript has been concerned with the vertical equilibrium assumption when modeling two-fluid-phase flow. The particular system analyzed is injection of supercritical CO_2 into a saline aquifer. The first element of the problem analyzed was the governing flow equations. The equations of mass and momentum transfer were derived from the standard microscale continuum equations. The averaging procedure employed converted these equations to two-dimensional differential equations at the lateral macroscale while full integration is over the vertical direction. The assumption of vertical equilibrium was employed to derive the megascale static condition for each fluid phase. Equations were developed that describe the two phase flow in three different regions: one fully saturated with brine, one with brine at residual saturation, and one with CO_2 at residual saturation.

The equations resulting from the derivation here are equivalent to previously published VE models (e.g. [22, 39]), despite the fact the starting point of the averaging procedure in those models was with the macroscale porous media equations. There are some other differences as well, notably the presentation in [22] described a drainage-only case and included additional processes, such as compressibility and flow across the top and bottom boundaries, that were not included in our model. However, by starting with the microscale equations, we are able to explicitly identify the key simplifying assumptions needed to arrive at the standard VE formulation described by others and implemented in the ECLIPSE simulator. This achievement implies that if the standard VE model fails to describe the system of interest, we can backtrack and identify the assumption or assumptions that were violated. This process that would not be possible from the formulation presented in previous studies alone.

The equations describing flow in these regions were solved using the ECLIPSE simulator run in fully three dimensional mode (ECL-3D) and in the vertical equilibrium mode (ECL-VE). The ECL-VE simulations were verified by both comparison to ECL-3D and to another vertical equilibrium model, VESA. In all cases, agreements were very excellent. The verified model was used to study the effect of caprock geometry on the lateral migration of a buoyant CO_2 plume. The variable height of the aquifer was synthesized as having a sinusoidal variability. Simulations were performed to examine the importance of the amplitude and period of the sinusoidal surface. These simulations demonstrated that CO_2 can be trapped in the caps at the surface such that migration is retarded or even halted, depending on the amount of CO_2 and the storage capacity of the caps.

The results of this analysis indicate that the VE formulation can be effective for simulating the CO_2 migration in a confined aquifer with variable thickness with reduced computer requirements in comparison to the full three-dimensional simulation. For example, the ECL-3D simulator took, on average, 55 times more time than the ECL-VE simulator to run the 2D simulations discussed in Section 3.2. The VE equations developed here describe the problem well, and the fact that all assumptions required to derive them are stated provides the opportunity to examine more complex problem (e.g., those with variable density or with capillary fringes between study regions).

References

[1] S. Bachu. Sequestration of CO_2 in geological media: Criteria and approach for site selection in response to climate change. *Energy Conv. Manag.*, 41(9):953–970, 2000.

[2] J. Bear. On the aquifer's integrated balance equations. *Advances in Water Resources*, 1(1):15–23, 1977.

[3] D. Bennion and S. Bachu. Dependence on temperature, pressure, and salinity of the IFT and relative permeability displacement characteristics of CO_2 injected in deep saline aquifers. In *Paper Number 102138-MS*. SPE Annual technical Conference and Exhibition, 24-27 September 2006, San Antonio, TX, 2006.

[4] M. Bickle, A. Chadwick, H. E. Huppert, M. Hallworth, and S. Lyle. Modelling carbon dioxide accumulation at Sleipner: Implications for underground carbon storage. *Earth and Planetary Science Letters*, 255(1-2):164–176, 2007.

[5] M. J. Bickle. Geological carbon storage. *Nature Geoscience*, 2(12):815–818, 2009.

[6] M. A. Celia and J. M. Nordbotten. Practical modeling approaches for geological storage of carbon dioxide. *Ground Water*, 47(5):627–638, 2009.

[7] R. A. Chadwick, P. Zweigel, U. Gregersen, G. A. Kirby, S. Holloway, and P. N. Johannessen. Geological reservoir characterization of a CO_2 storage site: The Utsira Sand, Sleipner, Northern North Sea. *Energy*, 29(9-10):1371–1381, 2004.

[8] H. Class, A. Ebigbo, R. Helmig, H. K. Dahle, J. M. Nordbotten, M. A. Celia, P. Audigane, M. Darcis, J. Ennis-King, Y. Q. Fan, B. Flemisch, S. E. Gasda, M. Jin, S. Krug, D. Labregere, A. N. Beni, R. J. Pawar, A. Sbai, S. G. Thomas, L. Trenty, and L. L. Wei. A benchmark study on problems related to CO_2 storage in geologic formations. *Computational Geosciences*, 13(4):409–434, 2009.

[9] K. H. Coats, J. R. Dempsey, and J. H. Henderson. Use of vertical equilibrium in 2-dimensional simulation of 3-dimensional reservoir performance. *Soc. Pet. Eng. J.*, 11(1):63–71, 1971.

[10] K. H. Coats, R. L. Nielsen, M. H. Terhune, and A. G. Weber. Simulation of three-dimensional, two-phase flow in oil and gas reservoirs. *Soc. Pet. Eng. J.*, Dec:377–388, 1967.

[11] E. C. Dahlberg. *Applied hydrodynamics in petroleum exploration.* Springer-Verlag, 1994.

[12] M. Dentz and D. M Tartakovsky. Abrupt-interface solution for carbon dioxide injection into porous media. *Transport in Porous Media*, 79(1):15–27, 2009.

[13] D. L. Dietz. A theoretical approach to the problem of encroaching and bypassing edge water. In *Proceedings of Akademie van Wetenschappen*, volume 56-B, page 83, 1953.

[14] C. Doughty. Investigation of CO_2 plume behavior for a large-scale pilot test of geologic carbon storage in a saline formation. *Transport in Porous Media*, 82(1):49–76, 2010.

[15] J. Drabbe and W. Badon Ghyben. Nota in verband met de voorgenomen putboring nabij Amsterdam. *Tijdschrift van het Koninklijk Instituut van Ingenieurs*, pages 8–22, 1889.

[16] J. Du Commun. On the cause of fresh water springs, fountains, etc. *American Journal of Science*, 14:174–176, 1828.

[17] G. T. Eigestad, H. K. Dahle, B. Hellevang, F. Riis, W. T. Johansen, and E. Øian. Geological modeling and simulation of CO_2 injection in the Johansen formation. *Comp. Geosci.*, 13(4):435–450, 2009.

[18] J. Ennis-King and L. Paterson. Role of convective mixing in the long-term storage of carbon dioxide in deep saline formations. *SPE J.*, 10(3):349–356, SEP 2005.

[19] F. Fayers and A. Muggeridge. Extensions to dietz theory and behavior of gravity tongues in slightly tilted reservoirs. *SPE Reservoir Engineering*, 5(4):487–494, 1990.

[20] R. A. Freeze and J. A. Cherry. *Groundwater.* Prentice-Hall, Englewood Cliffs, N.J., 1979.

[21] S. E. Gasda, J. M. Nordbotten, and M. A. Celia. Characterization of the effect of dipping angle on upslope CO_2 plume migration in deep saline aquifers. *IES Journal A: Civil and Structural Engineering*, 1(1):1–17, 2008.

[22] S. E. Gasda, J. M. Nordbotten, and M. A. Celia. Vertical equilibrium with sub-scale analytical methods for geological CO2 sequestration. *Computational Geosciences*, 13(4):469–481, 2009.

[23] S. E. Gasda, J. M. Nordbotten, and M. A. Celia. Vertically-averaged approaches for CO_2 injection with solubility trapping. *Water Resources Research*, 2011. in press.

[24] M. J. Golding, J. A. Neufeld, M. A. Hesse, and H. E. Huppert. Two-Phase gravity currents in porous media. *Journal of Fluid Mechanics*, pages 1–23, 2011.

[25] W. G. Gray, A. Leijnse, R. L. Kolar, and C. A. Blain. *Mathematical tools for changing spatial scales in the analysis of physical systems*. CRC, 1993.

[26] W. G. Gray and C. T. Miller. On the algebraic and differential forms of Darcy's equation. *Journal of Porous Media*, 14:in press, 2011.

[27] S. M. Hassanizadeh and W. G. Gray. Boundary and interface conditions in porous-media. *Water Resources Research*, 25(7):1705–1715, 1989.

[28] H. Hassanzadeh, M. Pooladi-Darvish, and D. W Keith. Accelerating CO_2 dissolution in saline aquifers for geological storage mechanistic and sensitivity studies. *Energy & Fuels*, 23(6):3328–3336, 2009.

[29] C. Hermanrud, T. Andresen, O. Eiken, H. Hansen, A. Janbu, J. Lippard, H. N. Bolås, T. H. Simmenes, G. M. G. Teige, and S. Østmo. Storage of CO_2 in saline aquifers-lessons learned from 10 years of injection into the Utsira Formation in the Sleipner area. *Energy Procedia*, 1(1):1997–2004, 2009.

[30] A. Herzberg. Die wasserversorgung einiger Nordsee bader. *J. Gasbeleuchtung and Wasserversorgung*, 44:815–819, 842–844, 1901.

[31] M. A. Hesse, F. M. Orr, and H. A. Tchelepi. Gravity currents with residual trapping. *Journal of Fluid Mechanics*, 611:35–60, 2008.

[32] M. A. Hesse, H. A. Tchelepi, B. J. Cantwell, and F. M. Orr. Gravity currents in horizontal porous layers: Transition from early to late self-similarity. *Journal of Fluid Mechanics*, 577:363–383, 2007.

[33] S. T. Ide, K. Jessen, and F. M. Orr. Storage of CO_2 in saline aquifers: Effects of gravity, viscous, and capillary forces on amount and timing of trapping. *International Journal of Greenhouse Gas Control*, 1(4):481–491, 2007.

[34] A. S. Jackson, C. T. Miller, and W. G. Gray. Thermodynamically constrained averaging theory approach for modeling flow and transport phenomena in porous medium systems: 6. Two-fluid-phase flow. *Advances in Water Resources*, 32:779–795, 2009.

[35] J. W. Johnson, J. J. Nitao, and K. G. Knauss. Reactive transport modelling of CO_2 storage in saline aquifers to elucidate fundamental processes, trapping mechanisms and sequestration partitioning. *Geological Society, London, Special Publications*, 233(1):107, 2004.

[36] R. Juanes, C. W MacMinn, and M. L Szulczewski. The footprint of the CO_2 plume during carbon dioxide storage in saline aquifers: Storage efficiency for capillary trapping at the basin scale. *Transport in porous media*, 82(1):19–30, 2010.

[37] A. Kopp, H. Class, and R. Helmig. Investigations on CO_2 storage capacity in saline aquifers-part 2: Estimation of storage capacity coefficients. *International Journal of Greenhouse Gas Control*, 3(3):277–287, 2009.

[38] A. Kumar, R. Ozah, M. Noh, G. A. Pope, S. Bryant, K. Sepehrnoori, and L. W. Lake. Reservoir simulation of CO_2 storage in deep saline aquifers. *Soc. Petrol. Eng. J.*, SPE 89343:336–348, 2005.

[39] L. W. Lake. *Enhanced Oil Recovery*. Englewood Cliffs, 1989.

[40] E. Lindeberg. Escape of CO2 from aquifers. *Energy Conversion and Management*, 38(Supplement 1):S235–S240, 1997.

[41] E. Lindeberg and D. Wessel-Berg. Vertical convection in an aquifer column under a gas cap of CO_2. *Energy Conv. Manag.*, 38(Suppl. S):S229–S234, 1997.
[42] C. Lu, S.-Y. Lee, W. S. Han, B. J. McPherson, and P. C. Lichtner. Comments on "Abrupt-interface solution for carbon dioxide injection into porous media" by M. Dentz and D. Tartakovsky. *Transport in Porous Media*, 79(1):29–37, 2009.
[43] C. W. MacMinn and R. Juanes. Post-injection spreading and trapping of CO_2 in saline aquifers: impact of the plume shape at the end of injection. *Computational Geosciences*, 13(4, Sp. Iss. SI):483–491, 2009.
[44] J. C. Martin. Some mathematical aspects of two phase flow with application to flooding and gravity segregation. *Prod. Monthly*, 22(6):22–35, 1958.
[45] B. Metz. *IPCC special report on carbon dioxide capture and storage*. Cambridge University Press, 2005.
[46] J. A. Neufeld, M. A. Hesse, A. Riaz, M. A. Hallworth, H. A. Tchelepi, and H. E. Huppert. Convective dissolution of carbon dioxide in saline aquifers. *Geophys. Res. Lett.*, 37(L22404):doi:10.1029/2010GL044728, 2010.
[47] J. A. Neufeld and H. E. Huppert. Modelling carbon dioxide sequestration in layered strata. *J. Fluid Mech.*, 625:353–370, 2009.
[48] H. M. Nilsen, P. A. Herrera, M. Ashraf, I. S. Ligaarden, M. Iding, C. Hermanrud, K.-A. Lie, J. M. Nordbotten, H. K. Dahle, and E. Keilegavlen. Field-case simulation of CO_2-plume migration using vertical-equilibrium models. In *Proceedings of GHGT10 (International Conference on Greenhouse Gas Control Technologies) Amsterdam, The Netherlands.*, 2010.
[49] J. M. Nordbotten and M. A. Celia. Similarity solutions for fluid injection into confined aquifers. *J. Fluid Mech.*, 561:307–327, 2006.
[50] J. M. Nordbotten and H. K. Dahle. Impact of the capillary fringe in vertically integrated models for CO_2 storage. *Water Resources Research*, 47(W02537):doi:10.1029/2009WR008958, 2011.
[51] J. M. Nordbotten, D. Kavetski, M. A. Celia, and S. Bachu. Model for CO_2 leakage including multiple geological layers and multiple leaky wells. *Environmental Science & Technology*, 43(3):743–749, 2009.
[52] G. S. H. Pau, J. B. Bell, K. Pruess, A. S. Almgren, M. J. Lijewski, and K. N. Zhang. High-resolution simulation and characterization of density-driven flow in CO_2 storage in saline aquifers. *Advances in Water Resources*, 33(4):443–455, 2010.
[53] A. Riaz, M. Hesse, H. A. Tchelepi, and F. M. Orr. Onset of convection in a gravitationally unstable diffusive boundary layer in porous media. *J. Fluid Mech.*, 548:87–111, 2006.
[54] Schlumberger Information Systems. ECLIPSE technical description. Report, Houston, TX, 2007.
[55] J. W. Sheldon and F. J. Fayers. The motion of an interface between two fluids in a slightly dipping porous medium. *Soc. Petrol. Eng. J.*, 2(3):275–282, 1962.
[56] Y. C. Yortsos. A theoretical analysis of vertical flow equilibrium. *Transport in Porous Media*, 18(2):107–129, 1995.

Appendix A. Averaging Theorems

To obtain the vertically averaged equations, we will make use of averaging theorems from the [3, (2, 0), 1] family [25] to transform three-dimensional mass and momentum conservation equations at the pore scale to vertically megascopic, laterally macroscopic two-dimensional porous media equations.

The averaging theorems to be employed involve a spatial integration region, Ω, of height b and cylindrical cross section of macroscale radius Δr. The orientation of the vertical direction is considered to be constant as denoted by a unit vector $\mathbf{\Lambda}$ that is tangent to the averaging cylinder axis. The region of a cylinder occupied by a phase denoted as the α phase is designated as Ω_α. The ends of the cylinder intersect the phases present. The portion of the end region area that intersects the α phase is denoted as $\Omega_{\alpha\text{end}}$.

The porous medium is composed of phases and interfaces between phases, as well as common curves where three phases meet. These are all referred to as entities. We will be concerned with averaging of phase properties. For convenience, a subscript will be used to indicate a microscale property while a superscript will denote a property averaged to the larger scale. The larger scale is macroscopic in the lateral directions and megascopic in the vertical direction and will be referred to as the averaged scale. In facilitating the integration from the microscale to the averaged scale, we will make use of an averaging operator notation defined according to

$$\langle F_\kappa \rangle_{\Omega_\alpha,\Omega_\beta,W} = \frac{\int\limits_{\Omega_\alpha} W F_\kappa \, \mathrm{d}\mathfrak{r}}{\int\limits_{\Omega_\beta} W \, \mathrm{d}\mathfrak{r}}. \tag{69}$$

where F_κ is a microscale property of entity κ being averaged to the macroscale, Ω_α is the domain of integration of the numerator, Ω_β is the domain of integration of the denominator, and W is a weighting function applied to the integrands in the definition of the averaging process. Omission of the third subscript on the averaging operator implies a weighting of unity. Although the bracketed quantity on the left side of the equation provides the needed specification of an average quantity, it can be clumsy to work with at times. Therefore, simplified notation will be employed for some averages that arise such that the intrinsic entity average is

$$F^\alpha = \langle F_\alpha \rangle_{\Omega_\alpha,\Omega_\alpha}, \tag{70}$$

and the density weighted entity average is

$$F^{\overline{\alpha}} = \langle F_\alpha \rangle_{\Omega_\alpha,\Omega_\alpha,\rho_\alpha}. \tag{71}$$

Additionally some macroscale properties will be presented with a double overbar for the subscript such as $F^{\overline{\overline{\alpha}}}$. This notation indicates that the macroscale average is defined in some unique manner for the variable of interest, and the definition will be provided. Finally, the density of an entity α (i.e., the volume fraction of a phase, the area per volume of an interface, or the length per volume for a common curve) is defined as

$$\epsilon^\alpha = \langle 1 \rangle_{\Omega_\alpha,\Omega} \tag{72}$$

One additional useful notation convention is the employment of $\prime$ to denote a two dimensional quantity for the lateral directions. For example, $\mathbf{f}^{\alpha\prime}$ is the lateral components of a vector property of entity α; ∇' is a gradient operator in the lateral directions; and $\partial'/\partial t$ is a partial time derivative of a quantity that depends only on the lateral spatial dimensions.

With these considerations, the averaging theorems may be expressed as follows [25]. For the average of a time derivative of a phase property theorem T[3, (2, 0),

1] is:

(73)
$$b\left\langle \frac{\partial f_\alpha}{\partial t} \right\rangle_{\Omega_\alpha,\Omega} = \frac{\partial'(b\epsilon^\alpha f^\alpha)}{\partial t} - \sum_{\kappa\in\mathcal{I}_{c\alpha}} b\langle \mathbf{n}_\alpha{\cdot}\mathbf{v}_\kappa f_\alpha\rangle_{\Omega_\kappa,\Omega} - \sum_{\text{ends}} b\langle \mathbf{n}_\alpha{\cdot}\mathbf{w}_{\text{end}} f_\alpha\rangle_{\Omega_{\alpha_{\text{end}}},\Omega}.$$

For the divergence operator, the averaging theorem D[3, (2, 0), 1] is expressed:

$$b\langle \nabla{\cdot}\mathbf{f}_\alpha\rangle_{\Omega_\alpha,\Omega} = \nabla'{\cdot}(b\epsilon^\alpha \mathbf{f}^{\alpha\prime}) + \sum_{\kappa\in\mathcal{I}_{c\alpha}} b\langle \mathbf{n}_\alpha{\cdot}\mathbf{f}_\alpha\rangle_{\Omega_\kappa,\Omega} + \sum_{\text{ends}} b\langle \mathbf{n}_\alpha{\cdot}\mathbf{f}_\alpha\rangle_{\Omega_{\alpha_{\text{end}}},\Omega}. \tag{74}$$

The gradient of a microscale quantity is averaged using theorem G[3, (2, 0), 1] as:

$$b\langle \nabla f_\alpha\rangle_{\Omega_\alpha,\Omega} = \nabla'(b\epsilon^\alpha f^\alpha) + \sum_{\kappa\in\mathcal{I}_{c\alpha}} b\langle \mathbf{n}_\alpha f_\alpha\rangle_{\Omega_\kappa,\Omega} + \sum_{\text{ends}} b\langle \mathbf{n}_\alpha f_\alpha\rangle_{\Omega_{\alpha_{\text{end}}},\Omega}. \tag{75}$$

When f_α is 1, eqns (73) and (75) become, respectively:

$$0 = \frac{\partial'(b\epsilon^\alpha)}{\partial t} - \sum_{\kappa\in\mathcal{I}_{c\alpha}} b\langle \mathbf{n}_\alpha{\cdot}\mathbf{v}_\kappa\rangle_{\Omega_\kappa,\Omega} - \sum_{\text{ends}} b\langle \mathbf{n}_\alpha{\cdot}\mathbf{w}_{\text{end}}\rangle_{\Omega_{\alpha_{\text{end}}},\Omega},, \tag{76}$$

and

$$0 = \nabla'(b\epsilon^\alpha) + \sum_{\kappa\in\mathcal{I}_{c\alpha}} b\langle \mathbf{n}_\alpha\rangle_{\Omega_\kappa,\Omega} + \sum_{\text{ends}} b\langle \mathbf{n}_\alpha\rangle_{\Omega_{\alpha_{\text{end}}},\Omega}. \tag{77}$$

Appendix B. Notation

Roman letters.

A	cross-sectional area of the averaging cylinder
b	height of a region over which integration occurs
F	general function
f	general function
$\mathbf{f}$	general vector function
$\mathbf{g}$	gravity vector
H	vertical coordinate of upper boundary of flow domain
h	vertical coordinate of interface between saturated brine and residual brine
h_i	vertical coordinate of interface between saturated brine and residual CO_2
I	identity tensor
$\mathcal{I}_{c\alpha}$	set of entities that form the surface bounding phase α
$\hat{\mathsf{K}}$	conductivity, inverse of resistance tensor R
$\hat{\mathsf{k}}$	relative permeability tensor
$\mathbf{n}_n$	outward normal vector from n phase on its boundary
$\mathbf{n}_w$	outward normal vector from w phase on its boundary
p	fluid pressure
$\mathbf{Q}^{\overline{\overline{\alpha}}\prime\prime}$	average lateral Darcy velocity of the α phase over the full height of the flow region
$\mathbf{q}^{\overline{\overline{\alpha}}}$	Darcy velocity averaged over a section, macroscale velocity scaled by the volume fraction
$\hat{\mathsf{R}}$	resistance tensor
S^α	vertically averaged saturation of phase α
s^α	saturation of α phase in a region
t	time
t	stress tensor

$\mathbf{v}$	velocity
W	weighting function
$\mathbf{w}_{\text{end}}$	velocity of the end of the averaging cylinder
z	vertical coordinate orthogonal to the bottom of the formation

Greek letters.

Δr	radius of averaging cylinder
ϵ	porosity
ϵ^n	volume fraction of the n phase
ϵ^w	volume fraction of the w phase
ϵ^α	volume fraction of an α phase
θ	constant slope angle of bottom of flow region relative to horizontal
$\mathbf{\Lambda}$	unit vector positive upward in the z direction normal to the base of the flow region
$\hat{\mu}$	dynamic viscosity
ρ	mass density
τ	viscous stress tensor
Ω	spatial domain of the cylindrical averaging volume
Ω_α	spatial domain of the α phase contained in a cylindrical averaging volume
$\Omega_{\alpha_{\text{end}}}$	surficial domain of the α phase in the surface at the end of a cylindrical averaging volume
Ω_κ	domain of entity κ appears here when κ is a boundary surface of a phase

Subscripts and superscripts.

bot	property evaluated at the bottom of the averaging region
H	evaluated at the top of the flow region where $z = H$
h	evaluated at the interface where $z = h$
h_i	evaluated at the interface where $z = h_i$
n	non-wetting, or CO_2 phase qualifier [subscript (microscale) and superscript (macroscale)]
$r$eff	effective relative permeability over the flow domain
res	residual
top	property evaluated at the top of the averaging region
w	wetting, or brine, phase qualifier [subscript (microscale) and superscript (macroscale)]
0	evaluated at bottom of flow domain where $z = 0$
1	refers to property of region 1, $0 \leq z \leq h_i$
2	refers to property of region 2, $h_i \leq z \leq h$
3	refers to property of region 3, $h \leq z \leq H$

Greek subscripts (for microscale) and superscripts (for macroscale).

α	qualifier referring to an entity [subscript (microscale) and superscript (macroscale)]
β	qualifier referring to an entity [subscript (microscale) and superscript (macroscale)]
κ	qualifier referring to an entity [subscript (microscale) and superscript (macroscale)]

Symbols.

∇'	surface gradient operator
$\nabla' \cdot$	surface divergence operator
$\partial'/\partial t$	partial time derivative in a surface
$^-$	above a superscript refers to a density weighted macroscale average
$^=$	above a superscript refers to a uniquely defined macroscale average with the definition provided in the text
$'$	vector tangent to a surface
$''$	surface tensor orthogonal to the z coordinate
$\langle F_\kappa \rangle_{\Omega_\alpha,\Omega_\beta,W}$	general average of a property associated with entity κ, $= \left(\int_{\Omega_\alpha} W F_\kappa \, \mathrm{d}\mathfrak{r} \right) / \left(\int_{\Omega_\beta} W \, \mathrm{d}\mathfrak{r} \right)$
$\langle F_\alpha \rangle_{\Omega_\alpha,\Omega_\alpha}$	macroscale volume average of an α phase property over the phase, $= F^\alpha = \left(\int_{\Omega_\alpha} F_\alpha \, \mathrm{d}\mathfrak{r} \right) / \left(\int_{\Omega_\alpha} \mathrm{d}\mathfrak{r} \right)$
$\langle F_\alpha \rangle_{\Omega_\alpha,\Omega_\alpha,\rho_\alpha}$	density weighted macroscale average of a property of a phase over that phase, $= F^{\overline{\alpha}} = \left(\int_{\Omega_\alpha} \rho_\alpha F_\alpha \, \mathrm{d}\mathfrak{r} \right) / \left(\int_{\Omega_\alpha} \rho_\alpha \, \mathrm{d}\mathfrak{r} \right)$

Tables

TABLE 1. Identification of characteristics of the three regions being considered.

Region	z	Phase	Saturation	Mobile?
1	$0 \le z \le h_i$	w	$s^w = 1$	yes
		n	$s^n = 0$	no
2	$h_i \le z \le h$	w	$s^w = 1 - s^n_{res}$	yes
		n	$s^n = s^n_{\text{res}}$	no
3	$h \le z \le H$	w	$s^w = s^w_{res}$	no
		n	$s^n = 1 - s^w_{\text{res}}$	yes

TABLE 2. Parameters used in all simulations.

Parameter	**Symbol**	**Value**	**Unit**
CO_2 density @ SC	ρ^n	696	kg/m^3
Brine density @ SC	ρ^w	1000	kg/m^3
CO_2 viscosity	$\hat{\mu}^n$	$5 \cdot 10^{-5}$	Pa·s
Brine viscosity	$\hat{\mu}^w$	$3 \cdot 10^{-4}$	Pa·s
CO_2 residual saturation	s^n_{res}	0.0947	-
Brine residual saturation	s^w_{res}	0.1970	-
Brine compressibility	β	$4.5 \cdot 10^{-10}$	Pa^{-1}
Porosity	ϵ	0.2	-
Permeability (isotropic & constant)	$\hat{K}$	100	mD
Aquifer slope	θ	0.57 (=1.0)	$\circ$ (%)

TABLE 3. Parameters used to define the aquifer and grid geometries in 2D application.

Parameter	**Symbol**	**Value**	**Unit**
Lateral extent (x)	L_x	20	km
Lateral extent (y)	L_y	1	m
Average thickness (z)	H_0	100	m
Lateral spacing (x)	Δx	20	m
Lateral spacing (y)	Δy	1	m
Average spacing (z)	Δz	2	m
Initial plume width (x)	ΔW_x	1000	m
Initial plume width (y)	ΔW_y	1	m

TABLE 4. Parameters used to define the aquifer and grid geometries in 3D application.

Parameter	**Symbol**	**Value**	**Unit**
Lateral extent (x)	L_x	15	km
Lateral extent (y)	L_y	15	km
Average thickness (z)	H_0	100	m
Lateral spacing (x)	Δx	50	m
Lateral spacing (y)	Δy	50	m
Average spacing (z)	Δz	2	m
Initial plume width (x)	ΔW_x	1000	m
Initial plume width (y)	ΔW_y	1000	m

Figures

Environmental Sciences and Engineering; University of North Carolina; Chapel Hill, NC 27599-7431, USA
E-mail: GrayWG@unc.edu

Uni CIPR, P.O Box 7810, 5020 Bergen, Norway. Current address: Department of Civil Engineering, University of Chile, Av. Blanco Encalada 2020, Santiago, Chile
E-mail: pherrera@ing.uchile.cl

Environmental Sciences and Engineering; University of North Carolina; Chapel Hill, NC 27599-7431, USA
E-mail: sgasda@unc.edu

Department of Mathematics, University of Bergen, Johs Brunsgt. 12, 5008 Bergen, Norway
E-mail: helge.dahle@math.uib.no

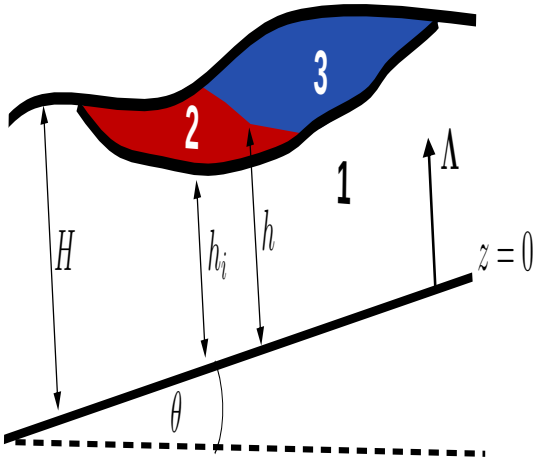

FIGURE 1. Aquifer system composed of brine (region 1), residual CO_2 and brine (region 2), and CO_2 and residual brine (region 3).

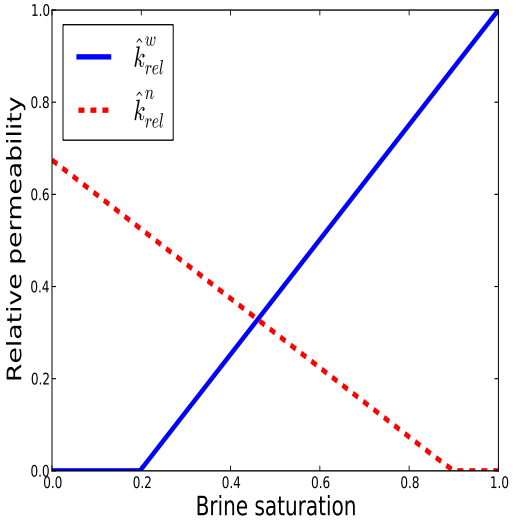

FIGURE 2. Relative permeability for CO_2 ($\hat{k}^n_{\text{rel}}$) and brine ($\hat{k}^w_{\text{rel}}$) as function of brine saturation. End points corresponds to residual CO_2 $s^n_{\text{res}} = 0.0947$ and residual brine $s^w_{\text{res}} = 0.1970$.

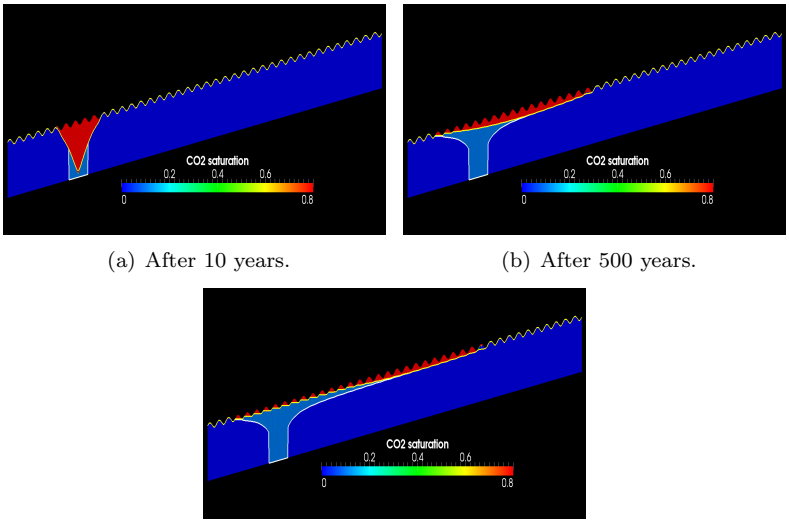

(a) After 10 years. (b) After 500 years.

(c) After 1300 years.

FIGURE 3. Comparison of simulated saturations with ECL-3D and plume thickness computed with ECL-VE for relative amplitude $a = 0.05$ and $n_x = 40$ periods. The white line indicates the position of the residual CO_2 interface (i.e. h_i) and the yellow line shows the boundary of the mobile CO_2 volume. Vertical scale is exaggerated by a factor 20.

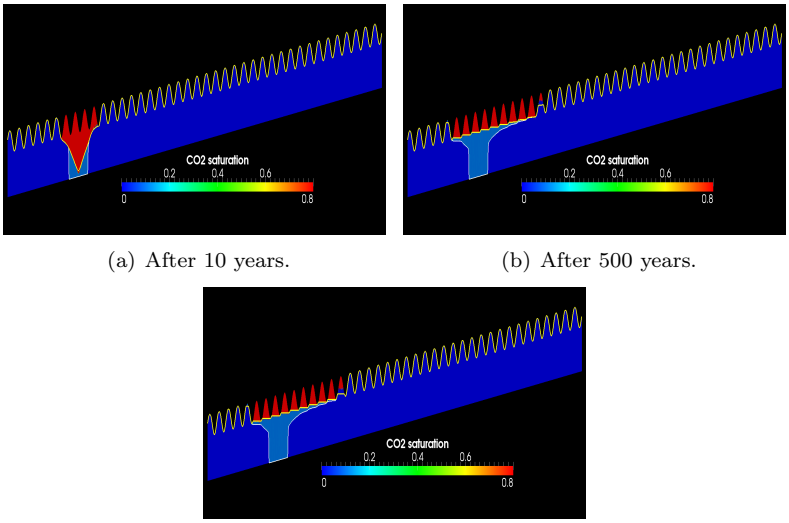

(a) After 10 years. (b) After 500 years.

(c) After 1300 years.

FIGURE 4. Comparison of simulated saturations with ECL-3D and plume thickness computed with ECL-VE for relative amplitude $a = 0.20$ and $n_x = 40$ periods. The white line indicates the position of the residual CO_2 interface (i.e. h_i) and yellow line shows the boundary of the mobile CO_2 volume. Vertical scale is exaggerated by a factor 20.

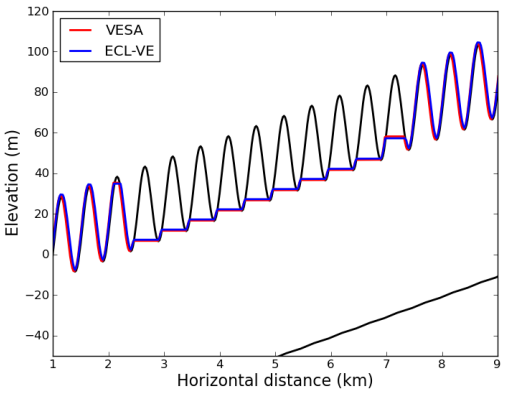

FIGURE 5. Comparison of numerical solutions computed with ECL-VE and VESA solvers for $a = 0.20$ and $n_x = 40$ after 1300 years. Red and blue lines show computed position of mobile CO_2 interface and the black lines correspond to the top and bottom of the aquifer. The vertical axis shows relative elevation with respect to an arbitrary datum level.

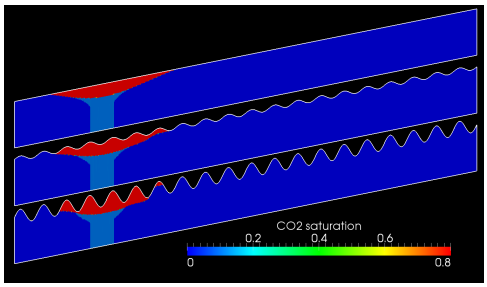

(a) After 100 years.

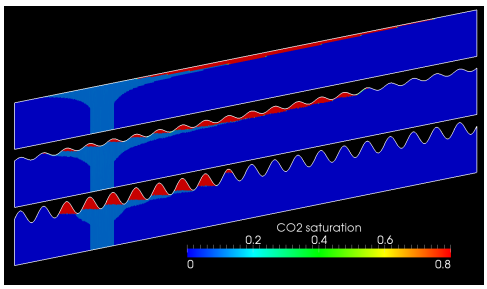

(b) After 1300 years.

FIGURE 6. Brine saturation for flat (top) and sinusoidal aquifers with wave number $n_x = 20$ and amplitude $a = 0.05$ (middle) and $a = 0.15$ (bottom). Light blue colors show areas with residual CO_2. Vertical exaggeration is 20×.

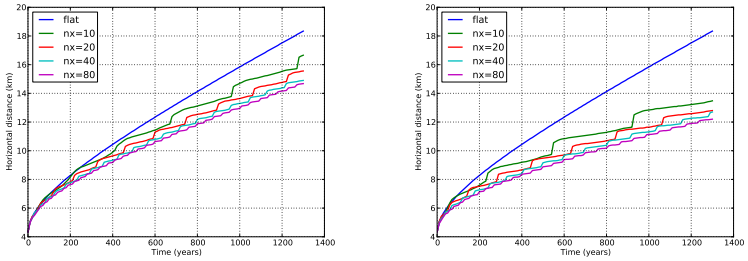

(a) $a = 0.05$ (b) $a = 0.10$

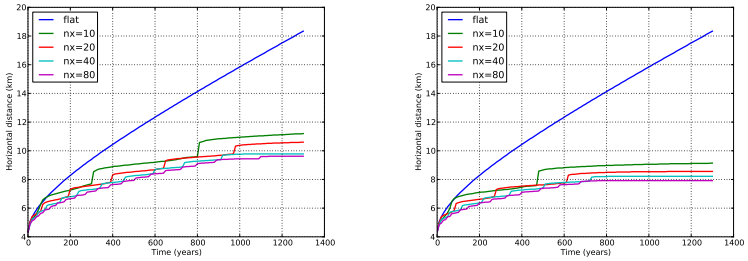

(c) $a = 0.15$ (d) $a = 0.20$

FIGURE 7. Plume tip position versus time for different values of relative amplitude a using the ECL-VE model.

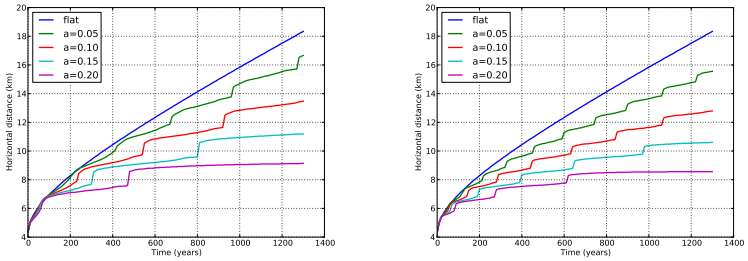

(a) $n_x = 10$ (b) $n_x = 20$

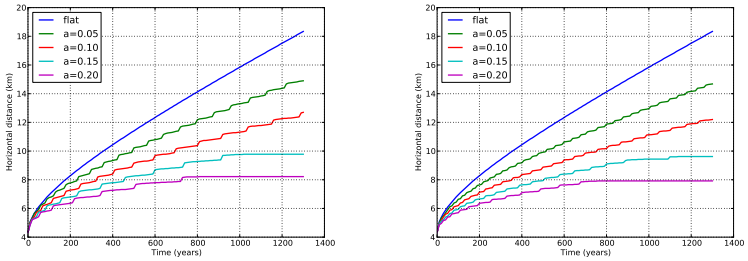

(c) $n_x = 40$ (d) $n_x = 80$

FIGURE 8. Plume tip position versus time for different values of the number of periods n_x using the ECL-VE model.

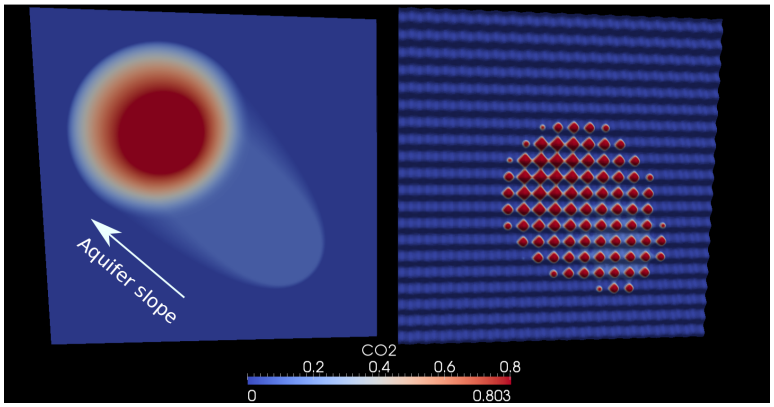

FIGURE 9. Top view of CO_2 saturations after 1000 years for flat (left) and sinusoidal (right) caprocks. Saturation values were mapped onto a three-dimensional grid from two-dimensional ECL-VE simulations.

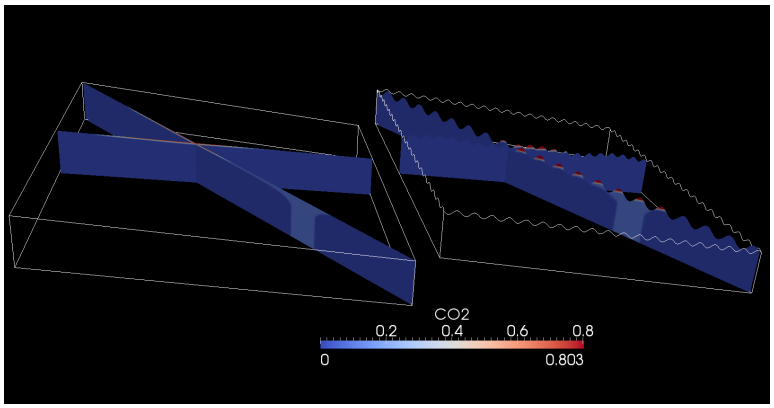

FIGURE 10. CO_2 saturation in vertical cross-sections after 1000 years for flat (left) and sinusoidal caprocks (right).